H2020-ICT-25-2016-2017

HYbrid FLying rollIng with-snakE-aRm robot for contact inSpection

HYFLIERS

D2.2

Prototypes of the hybrid robots

Contractual date of delivery	31 Mar 2022
Actual date of delivery	7 Oct 2022
Editor(s)	Guillermo Heredia (USE)
Author(s)	J. Parra (CATEC), P.J. Sanchez-Cuevas (CATEC), R. Schmid (WTR), V. Lippiello (CREATE), A. Viguria (CATEC)
Workpackage	WP2
Estimated person-months	42
Dissemination level	PU
Type	R
Version	1.0
Total number of pages	49

Abstract:

This document presents the final design of the HMR and HRA hybrid robots for contact inspection and its autonomous functionalities, as well as the evolution of the designs during the project. Several research concept prototypes that have been explored in the project are described also in the report.

Keywords:

Hybrid robot. Aerial robot. Satellite robot. Magnetic attractor. UT inspection. Miniature UT probe. Pipe inspection. Remote inspection. Refinery. Operations support. Ground station. Emergency behaviour.

Executive summary

This document describes the final design of the hybrid robot prototypes developed in the HYFLIERS project. These prototypes are the Hybrid Mobile Robot (HMR), for inspection of magnetic pipes, and the Hybrid Robot with Arm (HRA), for inspection of insulated and non-insulated pipes.

Deliverable D2.1 presented the initial design of both robots and their architecture and components. This document describes the evolution of the design of the HMR and HRA from D2.1 to the final designs. Several research concept prototypes that have been explored in the project are described also in the report.

The document also explains the autonomous functionalities that have been developed and tested for the HMR and HRA.

The references section includes a block with the HYFLIERS publications related to the design and autonomous functionalities of the hybrid robots,

With this deliverable concludes the exploratory research developed in HYFLIERS. The final integrated versions of the HMR and HRA robots and their components will be presented in D5.1 and D5.2.

Abbreviations and symbols

3D	Three-dimensional
AA	Articulated Arm
BLDC	BrushLess DC
CAD	Computer-aided Design
CNN	Convolutional Neural Network
CoM	Centre of Mass
DC	Direct Current
DoF	Degree of Freedom
EPM	Electro Permanent Magnet
FSR	Force-Sensing Resistor
GNSS	Global Navigation Satellite System
GPS	Global Positioning System
GPU	Graphics Processing Unit
HYFLIERS	Hybrid flying rolling with-snake-arm robot for contact inspection
HMR	Hybrid Mobile Robot
HRA	Hybrid Robot with Arm
IMU	Inertial Measurement Unit
IROS	International Conference on Intelligent Robots and Systems
ILC	Iterative Learning Control
MHYRO	Modular HYbrid RObot
PD	Proportional-Derivative
RANSAC	Random Sample Consensus
SDDRE	State-Dependent Differential Riccati Equation
SDRE	State-Dependent Riccati Equation
TPBVP	Two-Point Boundary Value Problem
TRL	Technology Readiness Level
UAV	Unmanned Aerial Vehicle
UT	Ultrasound Transducer
VP	Variable Pitch
VSLAM	Visual Simultaneous Localization and Mapping
WP	Workpackage

Table of Contents

List of figures

1. Introduction

This document is the second deliverable of workpackage 2. In the first deliverable D2.1 the initial design of the two hybrid aerial robots that are being developed in the project for pipe inspection was introduced as well as the general architecture and components of each one. This deliverable presents the final design of the hybrid robots.

The two approaches can be summarized as follows:

- **Hybrid Mobile Robot (HMR):** This robot is focused on a hybrid robot that can take-off, fly, land and move on a pipe to perform the inspection required by the end-users. This system is focused on the magnetic pipes inspection, and it is composed of an aerial vehicle adapted to the industrial environment and a satellite vehicle with the capability of crawling along the pipe to carry out the pipe inspection with the sensors mounted on-board.

- **Hybrid Robot with Arm (HRA):** The HRA is focused on magnetic and non-magnetic pipe inspection using a lightweight robotic arm with and UT probe. The system will be able to land on magnetic and non-magnetic isolated pipes and pipe racks. It consists of a modular aerial platform and different add-ons which will be used depending on the application. Due to HRA is targeting a wider range of application and more challenging scenarios (magnetic and non-magnetic pipes and pipe racks), this prototype is expected to have a lower technology readiness level (TRL). Instead, it is expected to generate a greater scientific impact driven by a more significant innovation.

With this deliverable it is concluded the exploratory research developed in HYFLIERS. The final integrated versions of the HMR and HRA robots and their components will be presented in D5.1 and D5.2.

The document is organized as follows: section 2 presents the HMR prototype, the evolution of its design and its autonomous functionalities. Section 3 deals with the HRA hybrid robot and presents its design evolution with the different prototypes developed in the project as well as the exploratory concepts that have been examined during the project. The document ends with the conclusions in section 4, and the references, which include a block with the HYFLIERS publications.

2. Hybrid Mobile Robot

The HMR focuses on the inspection of magnetic pipes. According to the concept presented in the D2.1 (Figure 1), the main novelty of the HMR is that it is composed of two semi-independent subsystems: the aerial platform and the self-propelled satellite. In accordance with the concept of operation, both subsystems have complementary functionalities to meet the end-users' requirements. First, the aerial platform carries and places the robotic satellite on the pipe to be inspected. Then, the satellite, also known as magnetic crawler, accomplishes the inspection itself using its inspection sensors.

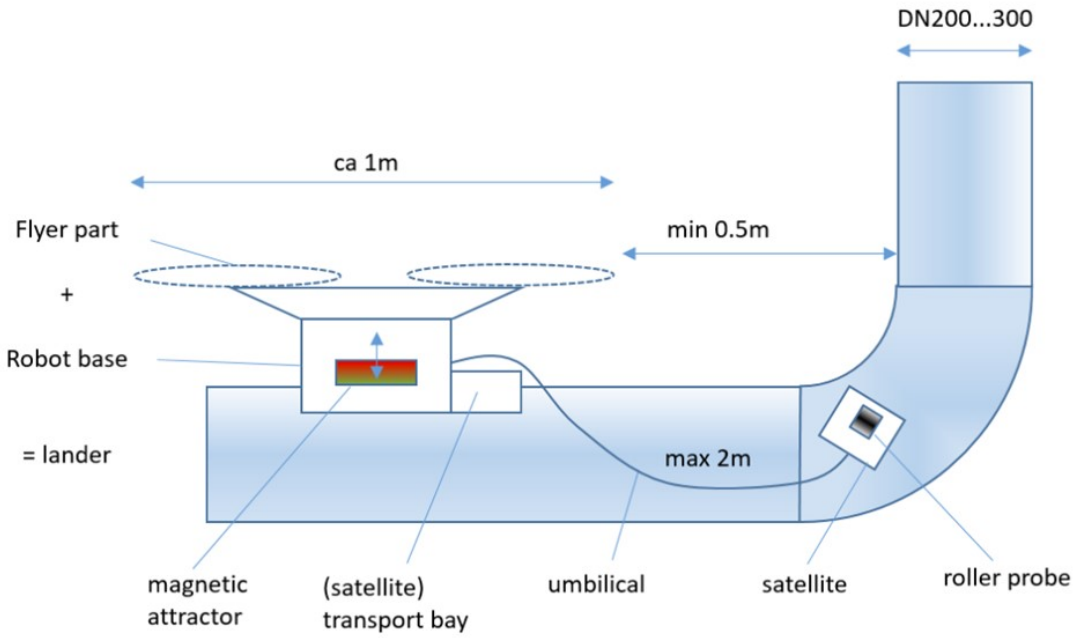

Figure 1 Block diagram of the HMR.

2.1. HMR prototype evolution

This deliverable presents how the Hybrid Mobile Robot (HMR) has evolved respect to the prototype presented in the D2.1. Unlike the first prototype of the HMR which was conceived as a first iteration to test all the robot functionalities and reach a minimum TRL, this new and final HMR prototype has been design considering all the project requirements and constraints.

The tests carried out with the first prototype helped to validate the main functionalities of each component and their autonomous functionalities, such as the landing gear or the localization system. The lessons learnt were used to make a design revision to include several improvements. On the other hand, the tests carried out have also served to learn about the onboard computer's processing capacity when running the necessary software.

The following subsections describe the final version of HMR and its evolution from the preliminary prototype presented in the D2.1. To do so and facilitate the system understanding, Figure 2 shows a brief description of the HMR.

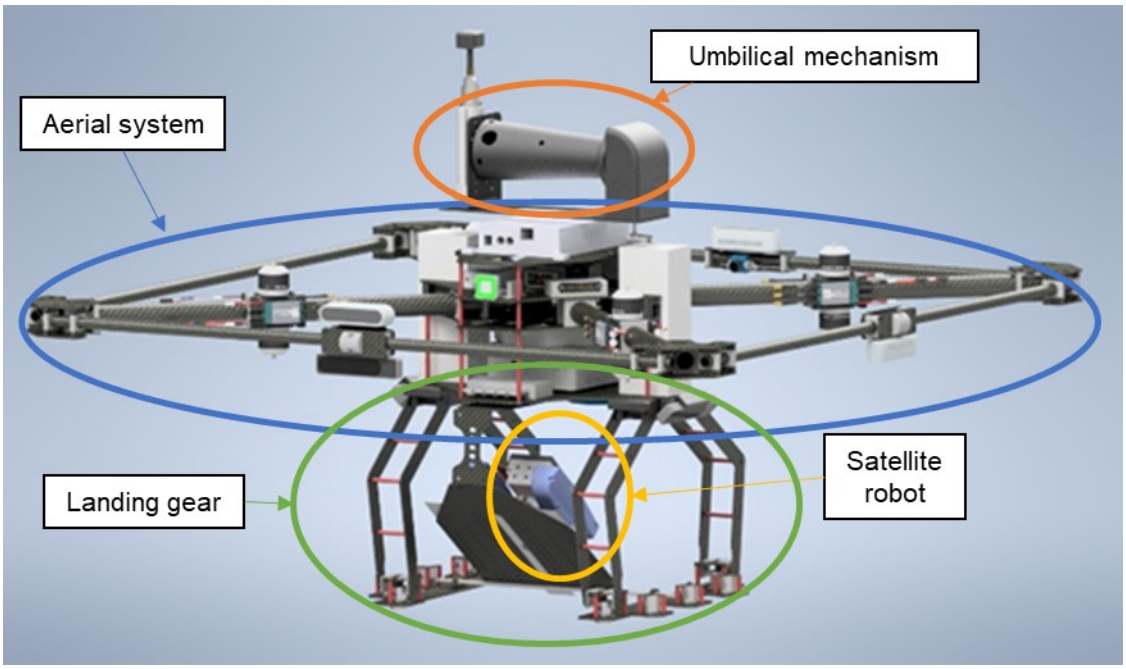

Figure 2. Final HMR concept.

According to Figure 2, the main components that compose the HMR are: the aerial system that includes the airframe, the propulsion system and the avionics, the localization system to localize the robot in a GNSS-denied environment, the magnetic landing gear to land on non-insulated pipes, the robotic satellite with the inspection sensor to collect the inspection measurements, and the umbilical mechanism which links the satellite with the rest of the system. As it was stated before, this deliverable presents the changes and improvements done in the HMR respect to the D2.1. Due to the inspection crawler has still not integrated in the HMR (pending along with the WP5) it has not experimented significant changes, therefore we are focusing the rest of the HMR components.

2.1.1. Aerial system

The HMR structure has been redesigned for the final prototype. The frame has been specifically designed for this project and has a different configuration than the previous one. The new structure has four arms instead of six, but it includes two more rotors, eight instead of six to increase robustness in case of a motor fail. In terms of energy consumption, this type of configuration is less efficient than others, as it does not take full advantage of the thrust force of the eight rotors. Still, for this project, due to the project's requirements, this is the configuration with which the most significant thrust force is achieved with the minimum possible size and weight. The propulsive system has been recalculated to guarantee the new payload requirements and motor distribution. The final version of the HMR mounts eight rotors T-Motor MN505-S with the KDE CF155 triple blade propellers and the T-Motor flame 60A ESCs.

The design of the final robotic hybrid robot is shown in Figure 3.

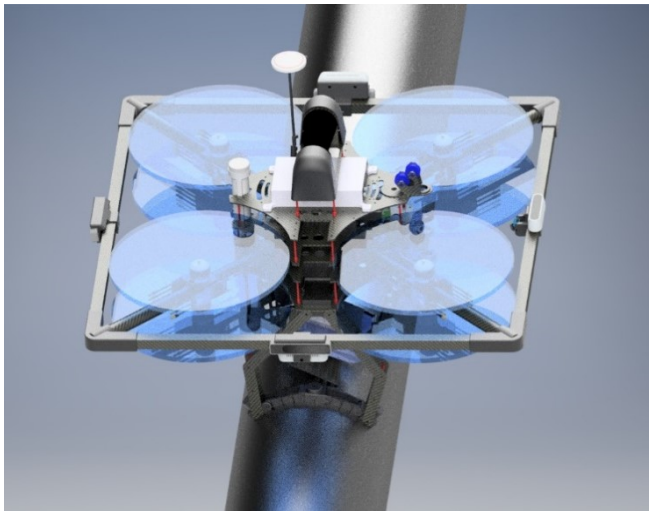

Figure 3. HMR final prototype.

Another relevant aspect of the new platform's design is the perimeter structure surrounding the drone, which has been designed to contain the necessary cameras and, on the other hand, to prevent against any possible lateral impact. Below (see Figure 4) is an image of the new platform showing the perimeter structure. The size of the surrounding case is 1m × 1m.

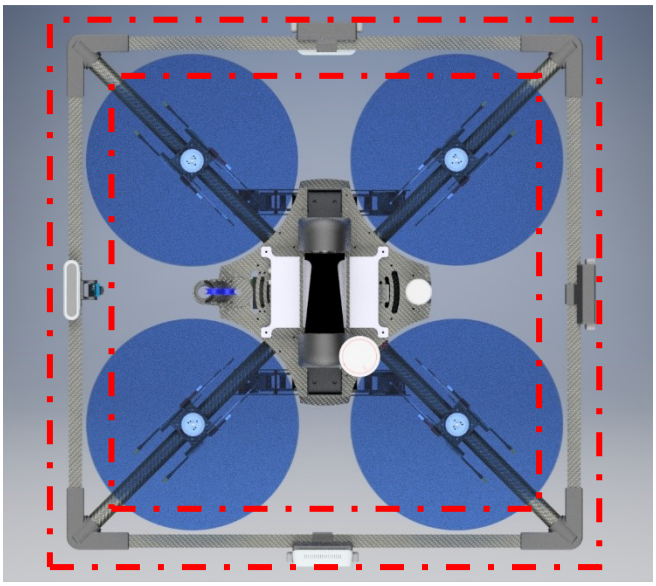

Figure 4. HMR new external structure.

The onboard computer of the final robot will be an Intel NUC8 i7. This device replaces the Jetson TX2 because installing a new set of cameras requires more processing power. The Jetson TX2 has neither the capacity to connect all the new components nor the necessary ports RealSense T265 cameras must each be connected to a separate port. NUC8 main specifications are the following:

- GPU: Radeon 540X, 2GB GDDR5
- CPU: Intel Core i7-8565U Quad-Core 64-Bit 4.6 GHz
- Memory: 8 GB LPDDR3-1866

- Storage: 256GB M.2 SSD
- Power: 15W

Figure 5. Intel NUC8 i7 computer.

2.1.2. Localization system and collision avoidance

The device chosen as a baseline for the localization system was the well-known and widely spread Intel RealSense T265. This camera provides a complete odometry message running an internal visual simultaneous localization and mapping (VSLAM) and it was tested on a series of flights to assess its performance feeding the position control loop in GNSS-denied environments. Although this device demonstrated a promising performance indoors, we realized that both eventual errors and vibrations were degrading the localization of the cameras a lot. To overcome this issue, a total of three RealSense T265 tracking cameras were installed in the robot and fused through a multi-sensor redundant localization algorithm (see Section 2.2.1 and [1]) that were able to exploit the triple redundancy of sensors and detect and isolate failing sensors.

Figure 6. RealSense T265 tracking camera.

The tracking cameras provides relative positioning solution, but not localization of the surrounding obstacles. For that purpose, three RealSense D435 depth cameras were integrated in the robot. The preliminary prototype used one of these cameras for landing and looking for obstacles in front of the robot. The new camera is used to detect possible obstacles that the hybrid mobile robot may encounter on top and built a multi-sensor occupancy map (described in D4.3 as a navigation support system).

Figure 7. RealSense D435 depth camera.

These components were located on the perimeter structure in particular positions to avoid occlusions in the FOV and achieve a better performance in both the odometry estimation and the situational awareness for obstacle detection. It was of course necessary to keep the center of gravity close to the geometrical center of the robot to facilitate the robot controllability and maneuverability.

Specifically, the RealSense D435 depth cameras are positioned towards the front, top and bottom. This situation is because flight restrictions have been imposed on the UAV make those directions the unique directions in which the robot could move. These restrictions are in the front, top, bottom and yaw directions. Because of this, obstacle detection is only required at the front, top and bottom. The position of these cameras is shown in the Figure 8.

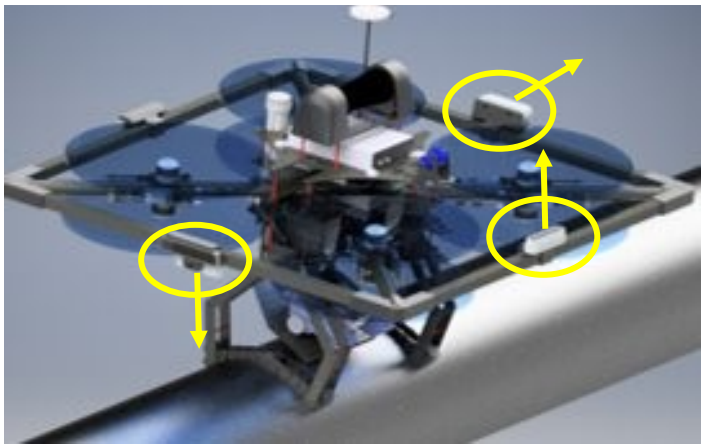

Figure 8. RealSense D435 position.

About the RealSense T265 tracking camera, they are similar to the RealSense D435. However, in this case, the position of these cameras was placed to obtain an estimation of position at different angles and obtain a redundant global position, helping to decrease the error in position obtained by a single camera.

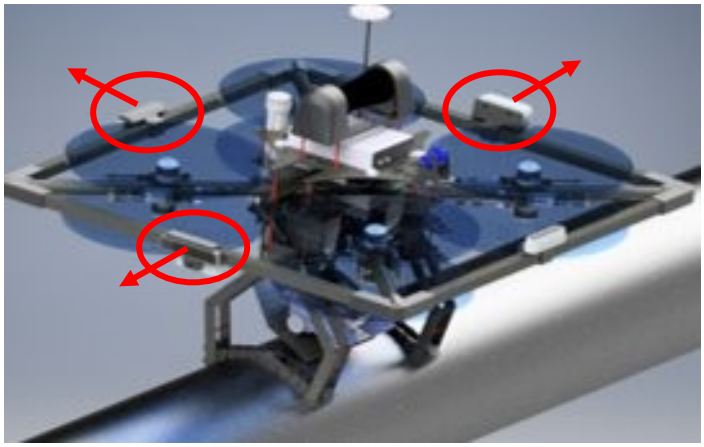

Figure 9. RealSense T265 position.

2.1.3. Magnetic landing gear for non-insulated pipes

To validate and assess the magnetic landing gear proposed in the D2.1 (see Figure 10), some experiments were carried out manually. The robot was positioned on the pipe to check its stability over the metallic pipe. The landing gear was able to keep the robot on the pipe in ideal conditions, however, we realized that if the drone's position was slightly rotated with respect to the pipe some magnets were losing the contact and the robot outbalanced.

Figure 10. HMR first landing gear prototype.

To overcome this issue, we develop a new landing gear (see Figure 11) with a chain system at the legs. This should solve the problem adherence because the flexibility of the system its capability to accommodate itself to the shape of the pipeline. On the other hand, as the chains are modular, each chain's link can be replaced by more magnets, making it possible to increase or decrease the adhesion power quickly.

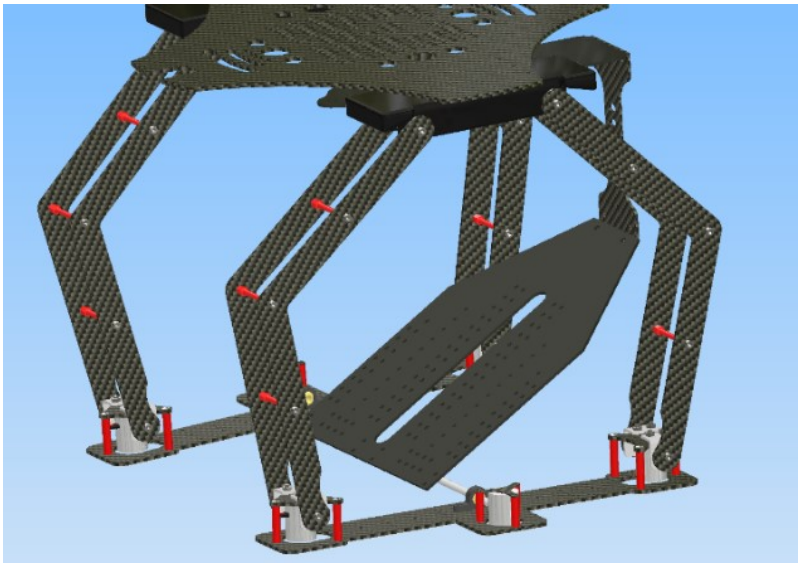

Figure 11. Final design of the landing gear.

The new landing gear was also equipped with a compliant mechanism between the proper legs and the airframe structure. This mechanism oversaw accommodating the landing gear when the robot lands on the pipe keeping the airframe in a horizontal way. This has a double advantage, first, it will facilitate the take-off from the pipe, and second, it will help the satellite operation keeping the crawler ramp always with the same angle respect to the pipe surface. To sum up, it was solving the problem of an off-centre landing. This compliant mechanism was created using ball joints that hold the bar that crosses both legs of the landing gear.

Both the misalignment situation and the off-centre landing were extensively tested with the new landing gear. An example is shown in Figure 12.

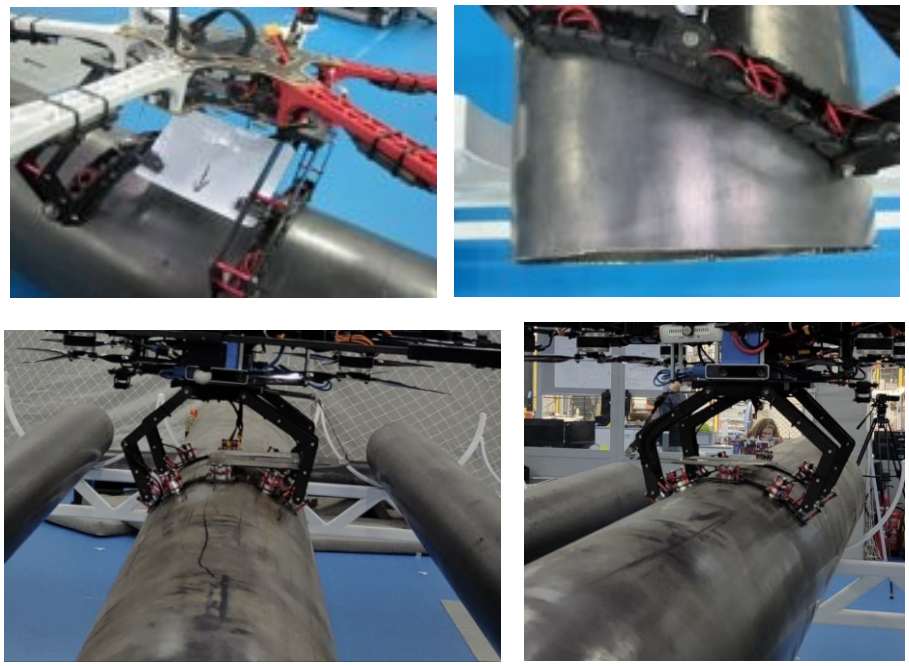

Figure 12. Landing gear on a pipe and in a non-aligned situation.

2.1.4. Satellite

The satellite in Figure 13 was built, its the design was outlined in D2.1.

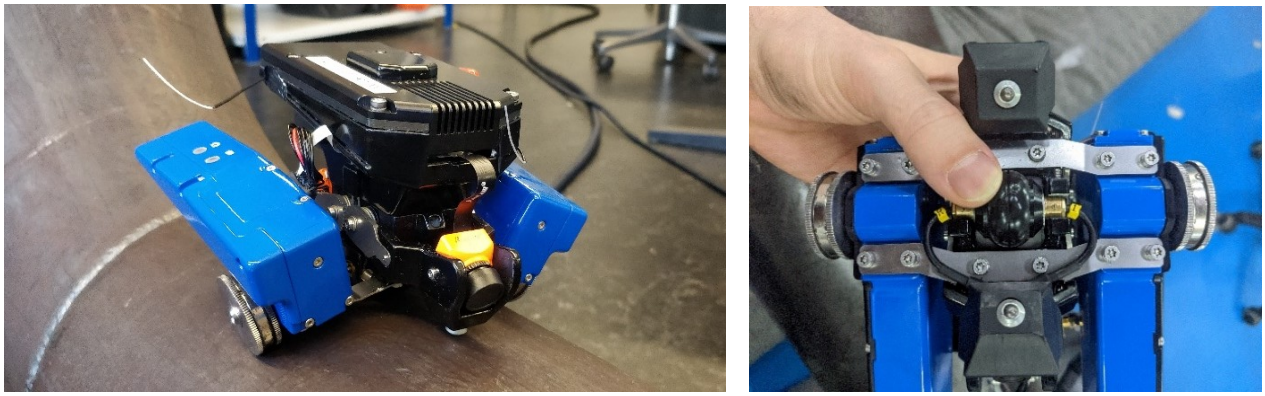

Figure 13. HMR satellite as built.

The most critical aspect was balancing the forces of the leaf spring suspension connecting the two drive units with the magnetic wheels to the central body. Tension on small-diameter piping would act against the magnetic force, potentially leading to loss oh contact. Too little tension on the other hand would not provide enough contact force to the Rollerprobe needed for a good signal. Similarly, the front and back arms had to be tensioned enough to keep the robot upright while driving. But the same tension will try to lift the Rollerprobe off the surface and act against the magnetic adhesion of the wheels. The proper balance was eventually verified by achieving a stable UT signal while moving on

an 8-inch pipe mock-up with elbow built for the purpose. Figure 14 shows such a line scan with a strong first and second backwall echo over the distance travelled.

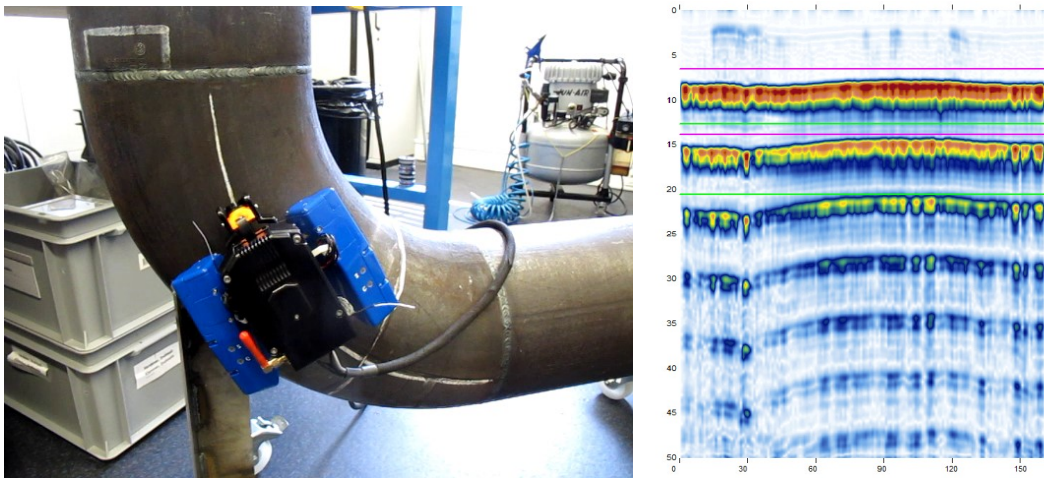

Figure 14. Satellite performing a UT line scan to verify good coupling.

2.1.5. Umbilical mechanism

Another component of the new platform is the cable winding system (see Figure 15). This is a servomotor-controlled thin ring to store the cable needed to connect the satellite with the power supply, the ultrasonic electronics, and the communication systems. The servomotor used for rolling the cable is a DYNAMIXEL with in torque control, so the cable is automatically extended or winded if the satellite goes farther or closer to the platform.

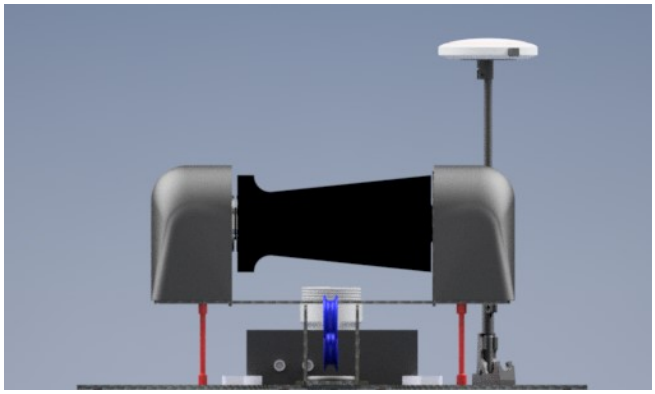

Figure 15. Cable rolling system.

2.1.6. Final HMR architecture

This section outlines the final HRM hardware architecture (Figure 16) and the line diagram (Figure 17) to be followed in the integration tasks during the WP5.

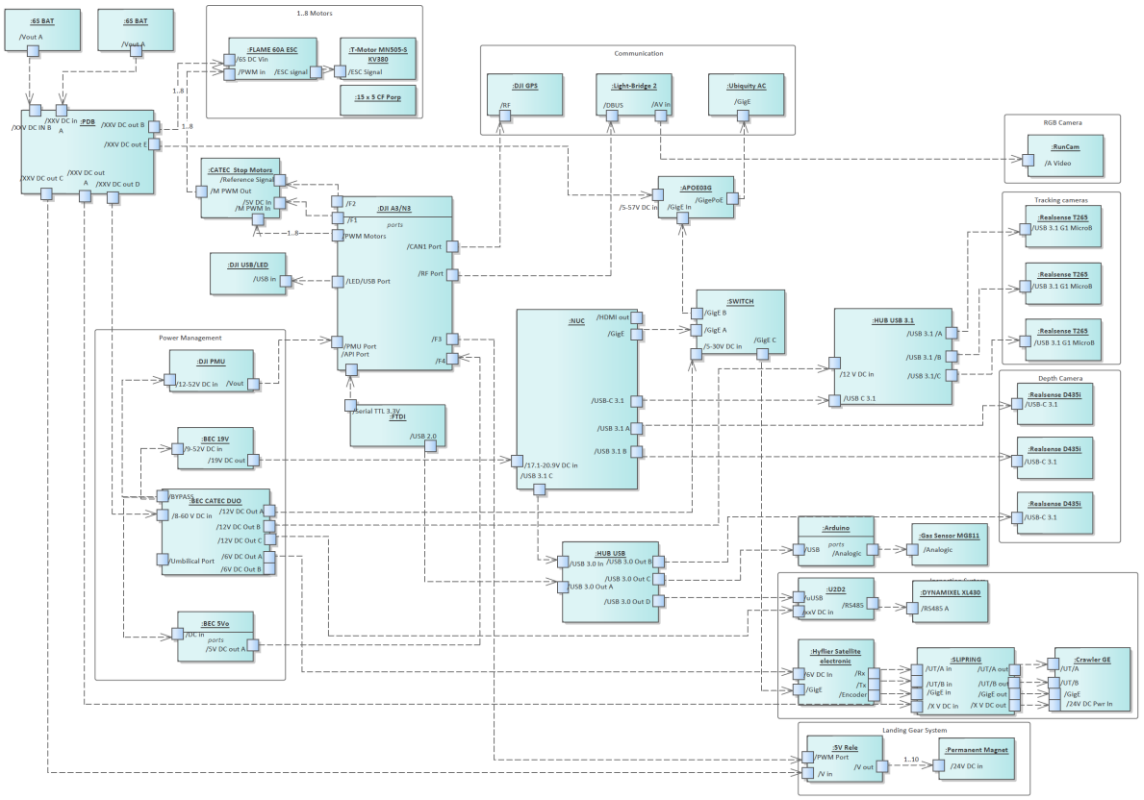

Figure 16. Final hardware architecture HMR.

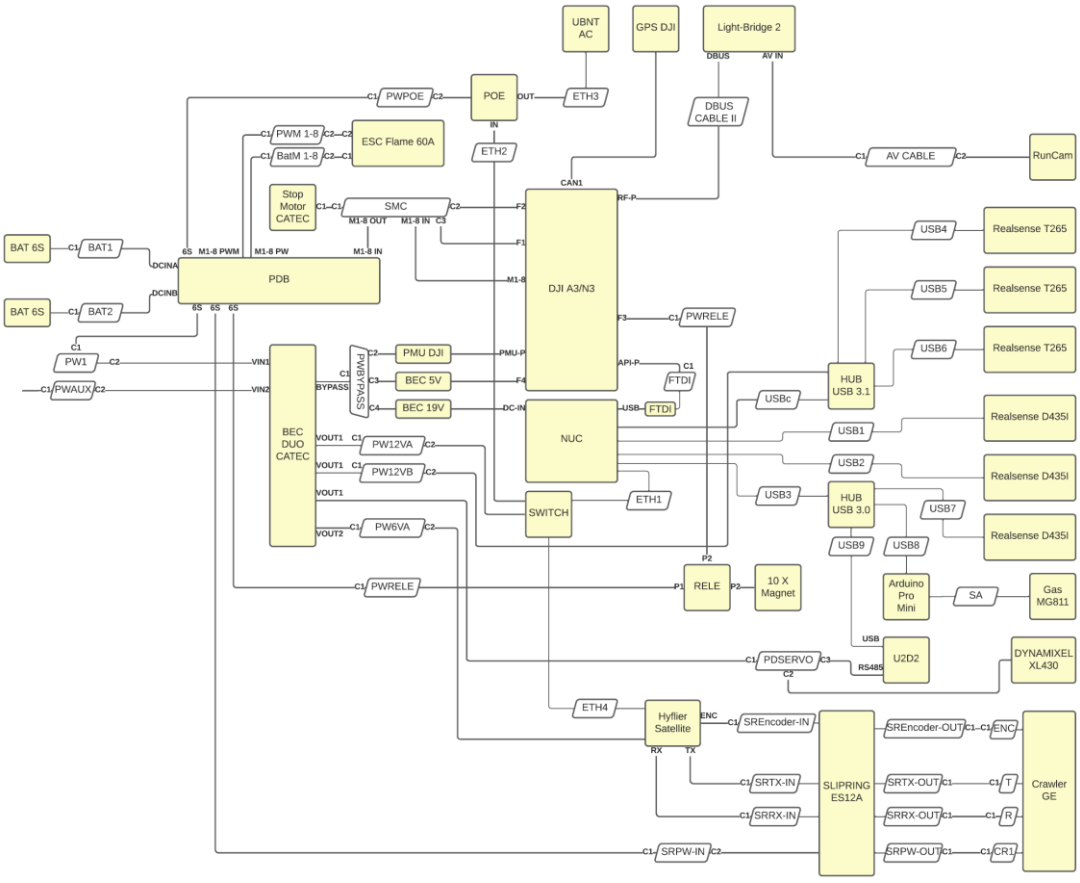

Figure 17. Line diagram HMR.

2.2. HMR autonomous functionalities

According to the concept of operation and project requirements collected along with the WP1, it was concluded that the HMR should embody two main autonomous functionalities. First, it is essential to have a robust localization system independent on the GNSS conditions to enable the assisted or autonomous flight mode. Second, the system should be able to differentiate and segment pipes to run the autonomous landing operation in a safe way. Apart from these main functionalities, the HMR intelligence will be composed of other functionalities like the ones provided by the mission controller, the mission state machine, the umbilical, and magnets controllers etc, however, those ones will be presented as proper software components in the D5.2 in their final form.

2.2.1. Robust multi-sensor redundant localization

The localization system fuses the information provided by three Intel RealSense T265 tracking cameras that is accomplishing an internal VSLAM algorithm. Each of them calculates its own odometry respect to an own reference system created in the initialization. Due to each camera is placed in different positions and with different orientations a transformation for each one of them to the centre of gravity is required. The position conversion of each camera to the aircraft's coordinate axes can be obtained using this transformation. In this way, the transition between the different cameras can be easily made. The following image shows the aircraft coordinate axes and the axes of each of the cameras.

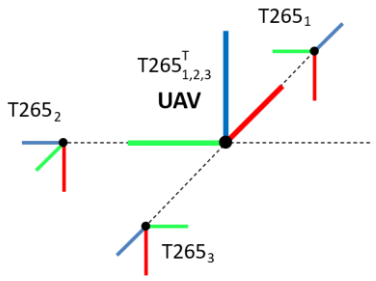

Figure 18. RealSense T265 coordinate axes.

The odometry measurements of the three tracking cameras are, then, fused using a multi-sensor filter based on the well-known Kalman Filter. This filtering technique can be divided into two distinct phases: prediction and update. The prediction phase uses the state estimated from the previous point of time to produce an estimate of the state at the current time. This phase is expressed as:

$$\begin{aligned}\hat{\mathbf{x}}_{k|k-1} &= \mathbf{F}_k\hat{\mathbf{x}}_{k-1|k-1} + \mathbf{B}_k\mathbf{u}_k \\ \mathbf{P}_{k|k-1} &= \mathbf{F}_k\mathbf{P}_{k-1|k-1}\mathbf{F}_k^{\mathsf{T}} + \mathbf{Q}_k\end{aligned} \qquad (2)$$

where $\hat{x}_{k|k-1}$ is the a priori state estimate at time k given observations up to k-1, $\mathbf{F}_k$ is the state transition model which is applied to the previous state estimation $\hat{x}_{k-1|k-1}$, $\mathbf{B}_k$ is the control-input model which is applied to the control vector $\mathbf{u}_k$, $\mathbf{P}_{k|k-1}$ is the a priori estimate covariance matrix and $\mathbf{Q}_k$ the covariance of the process noise matrix.
In the update phase, the innovation at time k, $\tilde{y}_k$, is multiplied by the optimal Kalman gain, K_k, and is combined with the previously estimated state to refine the state estimation:

$$
\begin{aligned}
\tilde{\mathbf{y}}_k &= \mathbf{z}_k - \mathbf{H}_k \hat{\mathbf{x}}_{k|k-1} \\
\mathbf{K}_k &= \mathbf{P}_{k|k-1} \mathbf{H}_k^{\mathsf{T}} \left(\mathbf{H}_k \mathbf{P}_{k|k-1} \mathbf{H}_k^{\mathsf{T}} + \mathbf{R}_k \right)^{-1} \\
\hat{\mathbf{x}}_{k|k} &= \hat{\mathbf{x}}_{k|k-1} + \mathbf{K}_k \tilde{\mathbf{y}}_k \\
\mathbf{P}_{k|k} &= \left(\mathbf{I} - \mathbf{K}_k \mathbf{H}_k \right) \mathbf{P}_{k|k-1} \\
\tilde{\mathbf{y}}_{k|k} &= \mathbf{z}_k - \mathbf{H}_k \hat{\mathbf{x}}_{k|k}
\end{aligned}
\tag{3}
$$

where $\boldsymbol{z}_k$ is the observation at time k and $\mathbf{I}$ is the identity matrix.

To extend the filter to *N* sensors that provide the same type of information, it is necessary to pay special attention to the terms $\mathbf{H}_k$ and $\mathbf{R}_k$. The observation matrix, $\mathbf{H}_k$, maps the state space into the observed space. Its dimensions are defined by the size of the state vector and the size of the observation vector. Regarding the covariance of the observation noise matrix, $\mathbf{R}_k$, it determines how much information from the measurement is used. If $\mathbf{R}_k$ is high, the filter considers that the measurements as not very accurate and further consideration will be given to the estimation of the model used. Its dimensions are defined by the size of the observation vector.

Although this work has used three redundant pose estimation sensors, the implementation of the redundant Kalman Filter can be extended to *N* sensors. In the following, the main equations for the implementation of this filter and the considerations taken are explained.

Our state vector and observation vector, x_k and z_k respectively, are shown in equation (4). As it can be seen, this filter is only used to estimate the aircraft's position and considers the use of the three on-board tracking cameras as observations.

Regarding the orientation estimation, the Inertial Measurement Unit (IMU) integrated into the aircraft autopilot is used. This is because the attitude estimation of the autopilot is sufficiently accurate and reliable, as well as operating at a high frequency, around 100 Hz. This allows to easily synchronize its measurements with the estimations of the proposed filter.

$$
\begin{aligned}
\mathbf{x}_k &= \begin{bmatrix} x & \dot{x} & y & \dot{y} & z & \dot{z} \end{bmatrix} \\
\mathbf{z}_k &= \begin{bmatrix} x_1 & y_1 & z_1 & x_2 & y_2 & z_2 & x_3 & y_3 & z_3 \end{bmatrix}
\end{aligned}
\tag{4}
$$

Due to the nature of the aircraft motion, the state transition matrix, $\mathbf{F}_k$, shall be defined from the equation of uniform rectilinear motion on each axis ($x_k = x_{k-1} + \dot{x}_{k-1}\Delta t$).

$$
\mathbf{F}_k = \begin{bmatrix}
1 & \Delta t & 0 & 0 & 0 & 0 \\
0 & 1 & 0 & 0 & 0 & 0 \\
0 & 0 & 1 & \Delta t & 0 & 0 \\
0 & 0 & 0 & 1 & 0 & 0 \\
0 & 0 & 0 & 0 & 1 & \Delta t \\
0 & 0 & 0 & 0 & 0 & 1
\end{bmatrix}
\tag{5}
$$

As mentioned above, the observation matrix, $\mathbf{H}_k$, maps the state space into the observed space. In other words, it converts the predicted state to the observation vector dimension:

$$
\mathbf{H}_k = \begin{bmatrix}
1 & 0 & 0 & 0 & 0 & 0 \\
0 & 0 & 1 & 0 & 0 & 0 \\
0 & 0 & 0 & 0 & 1 & 0 \\
\vdots & & & \ddots & & \vdots \\
0 & 0 & 0 & 0 & 1 & 0
\end{bmatrix}
\tag{6}
$$

Finally, the influence and shape of the observation matrix, $\mathbf{R}_k$, is analysed. This is a square matrix

providing information on the uncertainty of each measure. It is also known as the covariance matrix. Any covariance matrix is symmetric and positive semi-definite, and its main diagonal contains the variances.

This matrix is crucial in our redundant Kalman Filter, as it defines which sensors to consider and which ones to discard. In the case where the localization of one of the odometry sources starts to drift, its covariance will increase. This allows the filter to give priority to the motion model rather than the information received from such odometry source. In this way, a valid estimate will be achieved even when one or even several of the odometry sources have failed.

Apart from the previous Kalman implementation, we implemented an intelligent component to detect errors in the position estimation of the cameras using the covariance of their VSLAM processes and the divergence of their estimation with respect to the others. In this way, if it is detected that a camera is estimating incorrect position values, this data is discarded until its estimation is good again. Furthermore, these cameras are positioned at the front with a small upward tilt, at the left with a slight downward angle and at the right also with a slight downward tilt, thus having multiple points of view.

2.2.2. Depth-based pipe detector

The second goal of the perception algorithms is to estimate the pose of the pipe on which the hybrid system must land to perform the inspection. The point cloud from the downward depth camera is processed so that the target pipe is segmented and estimated. The algorithm is based on previous work by the authors [2] with some improvements. Figure 19 shows a diagram of the pipe segmentation algorithm used.

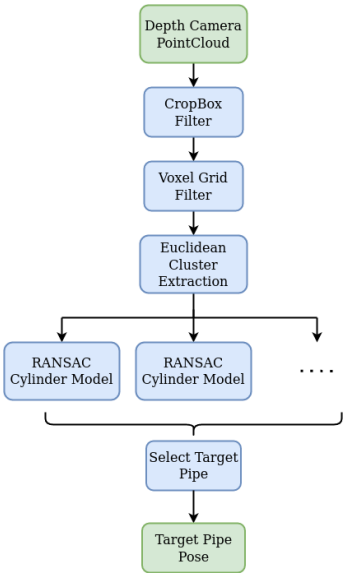

Figure 19. Perception algorithm diagram.

The perception algorithm can be divided into two parts: point cloud pre-processing, and target pipe pose estimation. During the first stage, several filtering steps are performed based on [26]. First, a Crop-Box filter is performed so that only the volume right under the aircraft is analysed. To this resulting volume, a Voxel-Grid filter is applied, so that the number of points is decreased to estimate the cylinder pose in the shortest possible time. The last step of this stage is an Euclidean cluster extraction, which separates the remaining elements in the point cloud, providing as an output every possible pipe in a different set of point clouds.

In the second stage of the pipeline, the target cylinder pose is estimated. For each cluster, surface

normal are estimated using the OpenMP standard [27]. This normal support the estimation of a model using Random Sample Consensus (RANSAC) [28]. RANSAC is an iterative method used to estimate the parameters of a mathematical model, a cylinder in our case, from a set of observed data that may contain outliers. The models obtained with RANSAC consist of the following coefficients: a point in the cylinder axis, the axis direction vector, and the estimated radius.

To check if the coefficients provided by the segmentation algorithm are consistent with previous detections, they are compared with a queue of previously obtained values. This allows ensuring a temporal consistency with the detected pipe and track it in consecutive frames. In contrast to the original algorithm, the cylinder to be landed on can be selected and tracked. This allows landing in more complex environments, where the most centred pipe is not always the target pipe. The full process of pipe detections is shown in Figure 20.

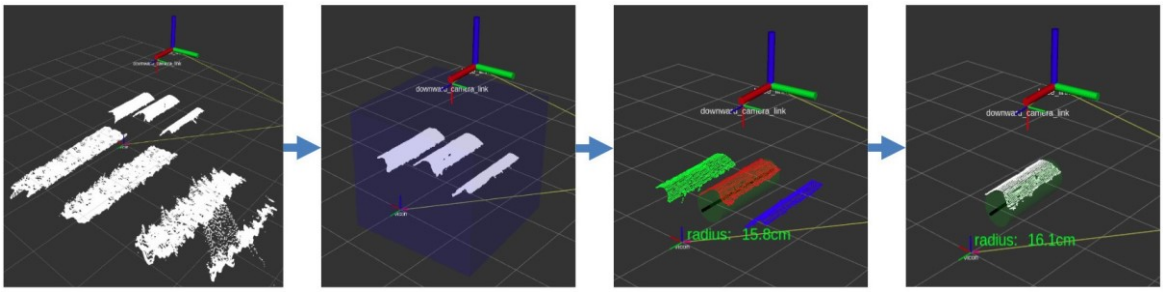

Figure 20. Segmentation and cylinder selection from D435i point cloud.

As previously mentioned, the improvements to the original algorithm mainly focus on guaranteeing consistency in pipe pose estimation. For this purpose, the curvature of the segmented pipe has also been tackled, by using its centroid and neighbourhood. To determine these neighbours efficiently, the input point cloud is split into smaller chunks using spatial decomposition techniques such as kd-trees. Then, closest point searches are performed in that space. The method used to estimate the curvature at a point p is to perform an eigen decomposition (i.e. compute the eigenvectors and eigenvalues) of the covariance matrix of the k-neighbourhood point surface patch.

In a 3D point cloud, a centroid is used to determine the covariance matrix of a certain point. From this three-dimensional covariance matrix, the eigen decomposition can be performed to know the curvature of the surface at a point. [29] The output surface curvature is estimated as a relationship between the eigenvalues of the covariance matrix as:

$$c = \frac{\lambda_0}{\lambda_0 + \lambda_1 + \lambda_2} \qquad (1)$$

where c is the curvature at the centroid of the cylinder, and λ_i is each eigenvalue of the three-dimensional covariance matrix, satisfying $\lambda_0 < \lambda_1 < \lambda_2$.

Figure 21. Pipe's pose calculation schema.

Two experiments have been performed on the same use case. From these, the average error in the pipeline estimation has been calculated. It should be noted that these flights have been carried out in manual mode, to also decouple the integration of the VICON localization with the control strategy, which could bring oscillations to the platform. During the execution of an autonomous mission, this error is more stable since the flight of the aircraft is more stable as well.

2.3. HMR validation

The validation of the new prototype and the new components included in it has been performed in the indoor CATEC testbed. Initially, we focussed on validating that the new drone flies correctly in manual mode and can approach the metal pipe rack without any disturbance problems. To ensure proper operation and achieve environmental conditions like the ones we could face outdoors, industrial fans were used to generate wind disturbances (see Figure 22). Furthermore, a cabling system was installed on top of the aerial robot as a safety measure, so we could avoid crashing the robot in case of problems.

Figure 22. Testing the HMR final prototype.

Finally, once the drone had been verified to be working correctly in flight, a series of flights were made, closing the control loop in hovering mode and moving it to specific waypoints. In this way, the control parameters were adjusted to achieve smooth movements during the mission.

Figure 23. HMR new prototype autonomous test.

Further experimentation of the aerial robot landing on pipes, deploying the satellite, and others, will be described in subsequent deliverables, like the ones involved in the WP5 in which all the integration details will be specified.

3. Hybrid Robot with Arm

The Hybrid Robot with Arm (HRA) is a hybrid robot which can fly, land on insulated or non-insulated pipes, and crawl over the pipe while the interest points in the pipe are inspected using a manipulator arm with a sensor in its end-effector. The HRA developed in HYFLIERS has a modular design, as presented in deliverable D2.1 and shown in Figure 24.

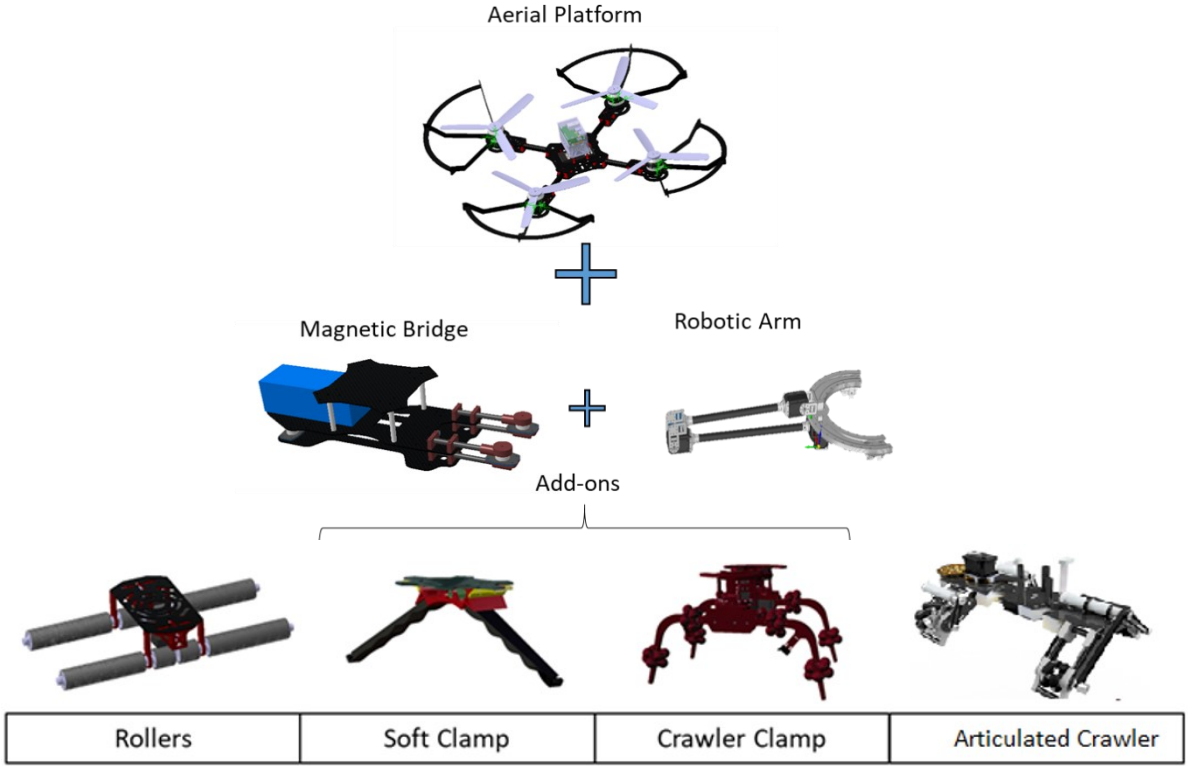

Figure 24. Modular Hybrid Robot Concept [D2.1].

This modular approach is based on a central aerial platform with a standard interface including a magnetic bridge for fast emergency response and different add-ons, which act as landing gear or ground system with different capabilities, to be able to operate in the different pipe configurations that appear in typical oil&gas factories. The robotic arm can be attached to the magnetic bridge or the add-on, depending on the design. The arm mounts at its end the pipe wall thickness sensor for inspection of the pipe, and the degrees of freedom of the arm allows it to reach different interest points over the pipe diameter.

Each add-on has been designed for different pipe configurations. The roller add-on allows to land and move over racks of pipes with small or no separation between them. The crawler clamp add-on has been designed to inspect individual pipes with a separation between them, where the HRA can land and move along the pipe. With the soft clamp the robot can land and attach firmly to individual pipes with small separation, allowing to land on inclined pipes up to 45º. The articulated crawler allows to land on single pipes, and move along it stabilizing the robot while moving.

3.1. HRA concept evolution

3.1.1. The Modular HYbrid RObot (MHYRO) prototype

MHYRO is a multi-modal aerial crawler robotic platform developed to implement the HYFLIERS HRA modular design in Figure 24 with the “Rollers” and “Crawler Clamp” add-ons, to test experimentally in the lab and outdoor mockups, gaining insights in their operation in real environments to improve the design. The MHYRO prototype is presented in [3], which won the IROS 2020 Best Application Paper Award.

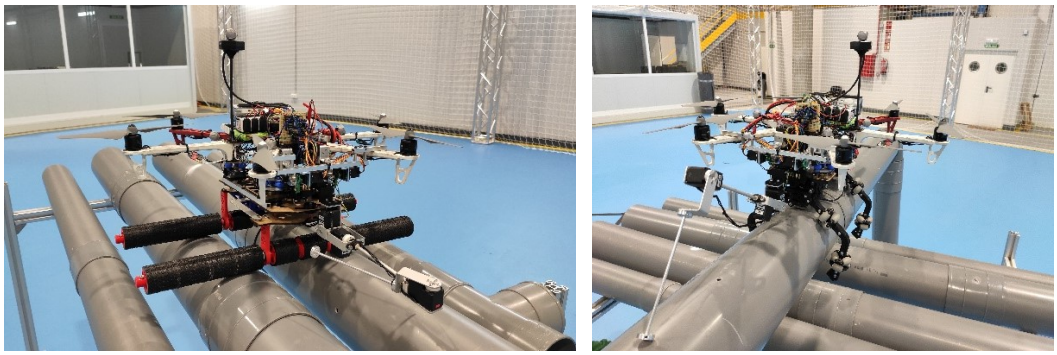

Figure 25. MHYRO prototype: a) with rollers add-on; b) with crawler clamp add-on.

MHYRO is designed to be adapted immediately before the flight taking into account the type of inspection and, after that, it is able to execute a repeated fly-crawl-fly cycle. It takes-off and flies from a specific area using the standard X-hexarotor layout configuration and controller. When it reaches the point of interest it is able to land over the isolated pipe or pipe rack in an autonomous way, and move along them to reach the inspection point, as illustrated in Figure 26.

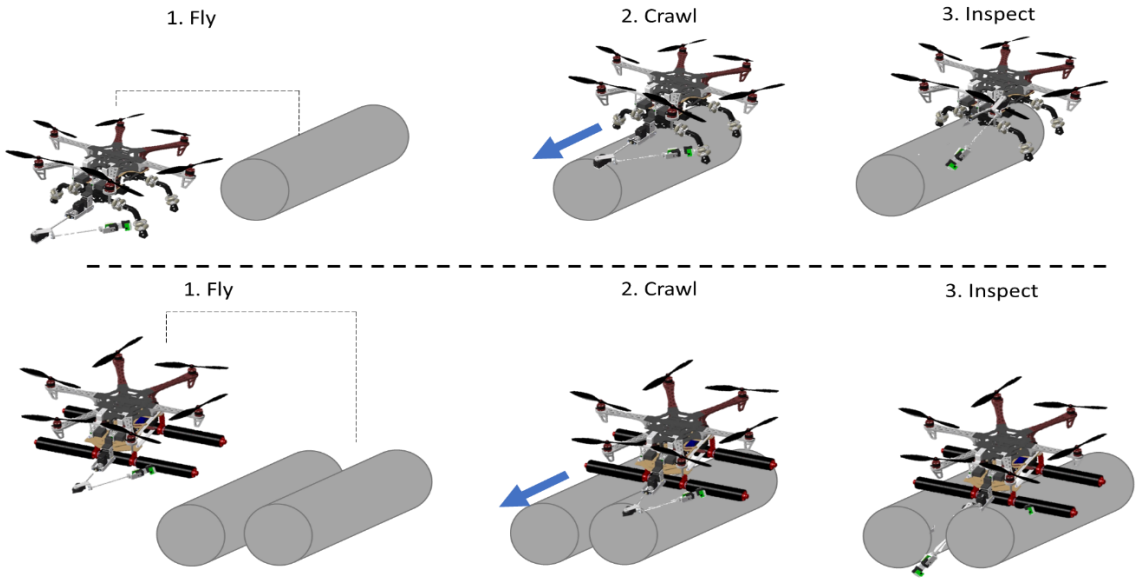

Figure 26. MHYRO concept of operation: approximation and landing on the pipe, crawling to the inspection point and inspection.

The MHYRO aerial platform has been adapted from a DJI F550 frame replacing the landing gear with a magnetic bridge which holds the rest of the robot. The concept of the magnetic bridge has been developed in a previous prototype which is described in [4]. In this first prototype an electromagnet device has been used (OpenGrab EPM), which combines the advantages of inductive electromagnets and permanent magnets, allowing its activation and deactivation with a pulse, while keeping the magnetic force without power consumption.

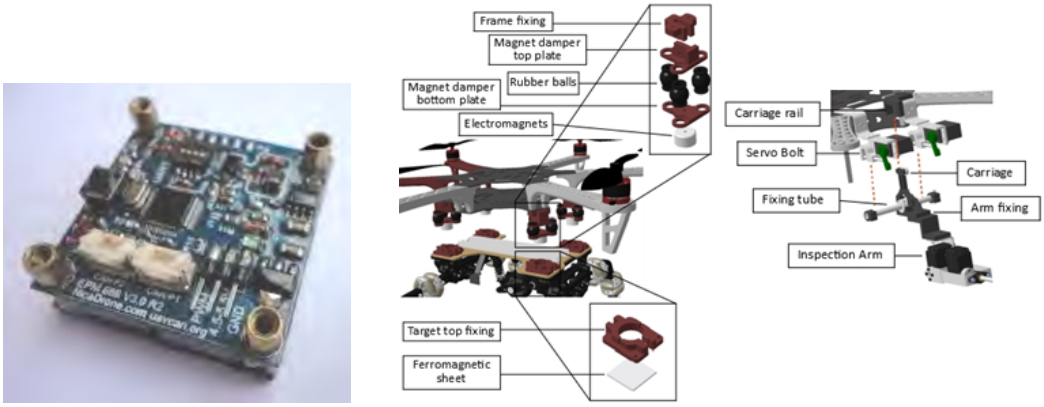

Figure 27. Magnetic bridge design: a) Initial design with OpenGrab EPM device; b) MHYRO adapted design.

From the experience of the first experimental tests, the design of the magnetic bridge in MHYRO has been adapted to have four damped magnets in its base, as shown in Figure 27b, and each add-on has a small ferromagnetic plate to maintain the subsystem in contact during normal operation. The aerial platform mounts DJI 2312E motors working with DJI 430 Lite ESC and DJI 9540 propellers. This motorization approximately provides a nominal thrust (50%) about 450 grams per rotor using a 4S battery (14.8V).

In the MHYRO prototype two interchangeable landing gears from the ones presented in Figure 24 have been designed and implemented. The first one, called Crawler-Clamp, is focused on the

inspection of isolated and non-magnetic pipes, while the second one, known as the Roller add-on, will be applied to inspect racks of pipes.

The Crawler-Clamp add-on is intended for deploying the platform on isolated pipes. It consists of two identical clamps placed on the frontal and rear side of the add-on and a central wheel. Each clamp has two custom L-shaped rigid legs assembled through an articulated joint to a central body which houses a 2:1 reduction ratio gearbox and an HSR-5980SG servo. Both legs engage the outer gears of the gearbox, so that the servo drives them symmetrically, producing the opening and closing movements of the clamp. Each leg has two omni-directional wheels to provide contact without constraining the displacement and turn of the platform along the longitudinal axis of the pipe. The central wheel is driven by a continuous rotation servo. A spring dumper provides compliance in the contact between the wheel and the surface when the clamps close around the pipe.

During the approach, clamps remain opened. Once a micro-switch installed at the bottom of the rear clamp detects contact, clamps close around the pipe at a low constant speed to allow a smooth attaching to the pipe. Then, the central wheel can be actuated to move the platform to the inspection point

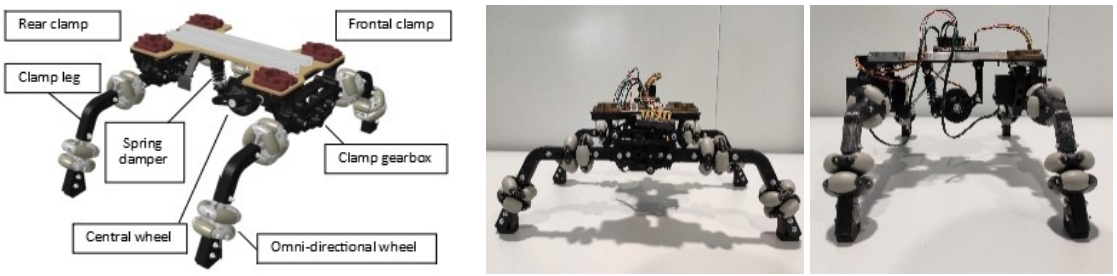

Figure 28. Crawler Clamp add-on: a) 3D CAD design; b) MHYRO implementation.

The Roller add-on is designed to perform pipe rack inspections. This add-on allows passive docking after landing, the propulsion system of the aerial platform can be turned off to perform inspection tasks by movement of the rollers (see Figure 29a). In addition, this design does not need stabilization control and the landing can be easily done by aligning the rollers on the pipe. The rolling base in MHYRO has been implemented with a continuous rotation servo (Power HD AR-3600HB 6.7kgcm, 71rpm) to provide longitudinal movement through a gear system and with a HerkuleX DRS-0602 (77kgcm) servo to control the direction by means of a crank-crank mechanism, as shown in Figure 29b. The turning mechanism is aided by a set of ball bearings that facilitate movement.

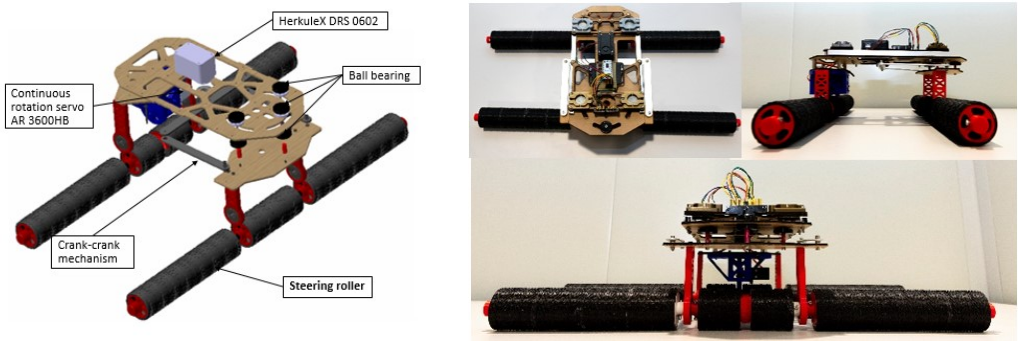

Figure 29. Roller add-on: a) 3D CAD design; b) MHYRO implementation.

3.1.2. Articulated arm prototypes

The HRA mounts an articulated arm which has the ultrasonic sensor probe installed at its end-effector, so that the degrees of freedom of the arm allows it to reach different points of the pipe that need to be inspected. The HRA arm has been developed in WP3 and it is described in D3.1.

For testing of the different HRA prototypes, several test designs of the articulated arm have been designed and implemented. These arm prototypes are described in the following.

AA1 articulated arm prototype

The AA1 prototype, described in [5], is an arm with a kinematic 2-DOF Cartesian base (XY–axes) that carries a 1-DOF compliant joint arm equipped with a gripper and a deflection-based force-torque sensor. Figure 30 shows the designed prototype. The proposed morphology is intended to improve the positioning accuracy of the end effector while reducing the inertia, torque and weight of the actuators, since the Cartesian base supports most of the weight of the robotic manipulator (0.85 kg weight, 1 m reach, and 10 cm/s speed). The elastic deflection sensors integrated in the compliant joint and in the fore-arm link are used to estimate and monitor the force (XZ–axes) and torque (pitch) exerted by the manipulator over the aerial platform.

The Cartesian manipulator is divided into the five parts identified in Figure 30a: X–axis linear guide (base), Y–axis linear guide, servo actuator, compliant arm and battery counterweight mechanism. The 2-DOF Cartesian base is built from the igus® NS-01-17-600 (X–axis) and NS-01-17-300 (Y–axis) linear guides, using three NW-02-17 carriages to support the mobile parts. Two 22 mm Ø timing pulleys are placed at the tip of both linear guides to transmit the motion of the Pololu micro metal gear motors to the timing belts, measuring the rotation angle with a Murata SV01A potentiometer and with the magnetic encoder of the micro-motors. The linear displacement of the Cartesian base relative to an initial position is obtained from the rotation angle and the number of turns given by the encoder (6 pulses per revolution at the micro motor shaft, 1500 pulses per turn at the output shaft of the gearbox). The battery counterweight is supported by a C-shaped aluminium frame that can slide along the X–axis linear guide and move in synchronization with the Y–axis structure, but in the opposite direction when it is attached to the X–axis timing belt.

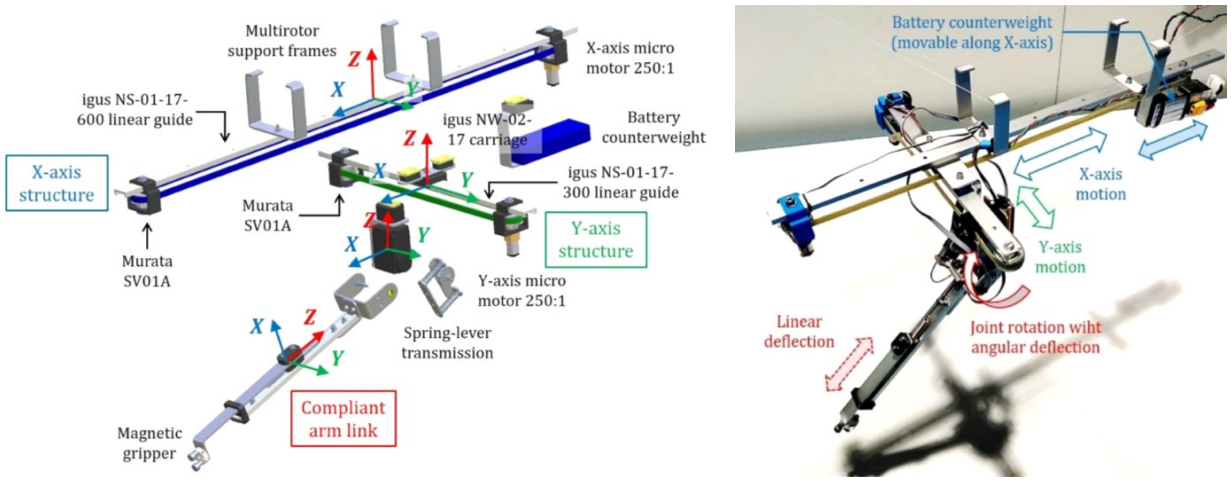

Figure 30. AA1 articulated arm prototype: a) 3D CAD design; b) developed arm.

The compliant arm employs a Herkulex DRS-0101 servo and a spring-lever transmission mechanism (1.4 Nm/rad stiffness) that allows the estimation and control of the torque from the deflection measurement, integrating an AS5048 magnetic encoder to obtain the deflection angle at 500 Hz with

0.2º accuracy. This configuration allows for force estimation with an estimator that uses both the linear and angular deflections of the arm. Modelling and control of the arm is described in [5], as well as force control experiments.

AA2 articulated arm prototype

The AA2 manipulator, described in [3], was adapted for the inspection of pipe structures, allowing the access to different points of the contour, or the insertion of the end effector in the space between an array of pipes, as Figure 31 illustrates. The manipulator is a 3-DOF lightweight robotic arm in the usual upper arm-forearm configuration, with two joints at the shoulder (pitch and yaw), and one at the elbow (pitch). The arm is built with the Herkulex DRS-0101 smart servos, and a customized aluminum frame structure. The arm implements partially the anthropomorphic kinematics described in [30], but removing the shoulder roll joint, with the same position/trajectory control schemes based on inverse kinematics that relies on the servo controller.

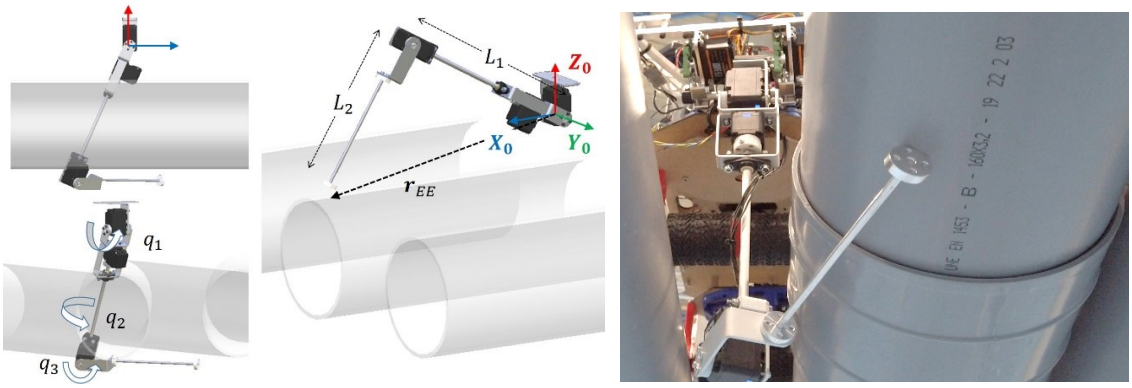

Figure 31. AA2 robotic arm: a) Different poses of AA2 in a scenario with pipes. Reference frame, joint variables, and link lengths; b) developed AA2 inspecting a point in a pipe.

AA3 articulated arm prototype

The AA3 prototype, described in [6] and depicted in Figure 32, adds several degrees of freedom to the AA2 configuration to gain dexterity for reaching inspection points in the different parts of the pipe, with a total of 6 DOF. It consists of a lightweight robotic arm with three joints for end-effector positioning, two joints for wrist orientation, and an actuated linear guide system that allows the transverse displacement of the arm to access the gap between the pipes. A customized frame structure manufactured in anodized aluminium supports the Herkulex DRS-0101 servos of the shoulder and elbow joints, as well as the customized micro servo actuators built with the Pololu micro metal gear motors used in the wrist joints. The end effector section comprises three polymer frame parts (the bearing and the cases), the Murata SV01-A potentiometer used to measure the rotation angle, the Pololu micro metal gear motor 250:1, and the microcontroller board. The actuator, weighting 25 grams, with a size of 22 × 22 × 35 mm, provides a maximum torque around 0.2 Nm with a maximum speed of 300 deg/s.

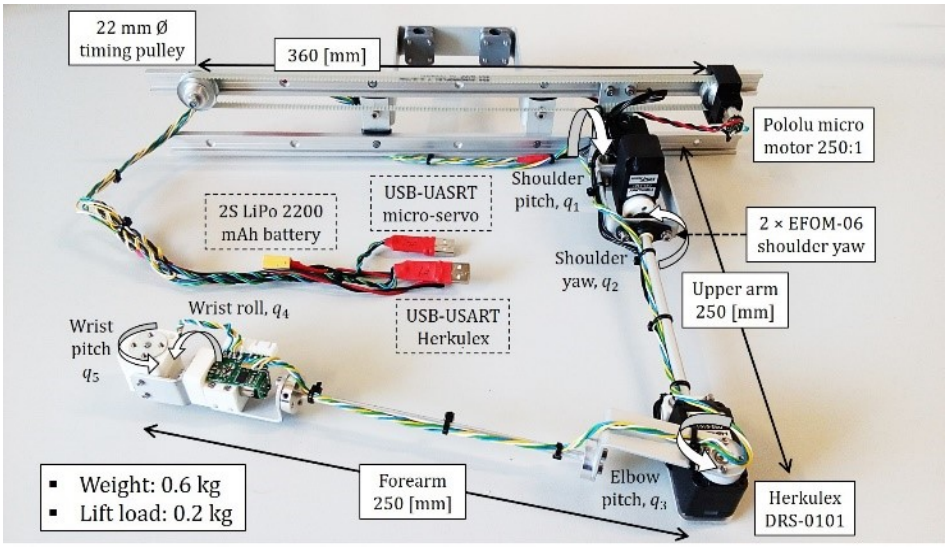

Figure 32. AA3 robotic arm, with 5-DOF arm supported by a 1-DOF linear guide system.

3.1.3. Soft clamp

The soft clamp is a landing gear add-on that allows to attach the HRA robustly to the pipe during inspection and maintenance tasks. The design is based on a soft gripper which uses soft materials combined with actuators. Unlike rigid mechanical systems, soft materials offer beneficial properties for the landing system, as the ability of adapting to pipes of different diameters and the capability of absorbing the impact on the pipe while landing, preventing the robot from bouncing and falling.

Two different designs have been introduced in D2.1. The first of them is a preliminary concept model used to strongly attach the UAV pipe on the landing, which is described in [7]. The second design is the mobile soft clamp which focuses on enabling this soft gripper add-on to creep over the pipe, so that the HRA can move along the pipe while inspecting. Preliminary developments of this design were included in D2.1, and the evolved prototype is included here and described in [8].

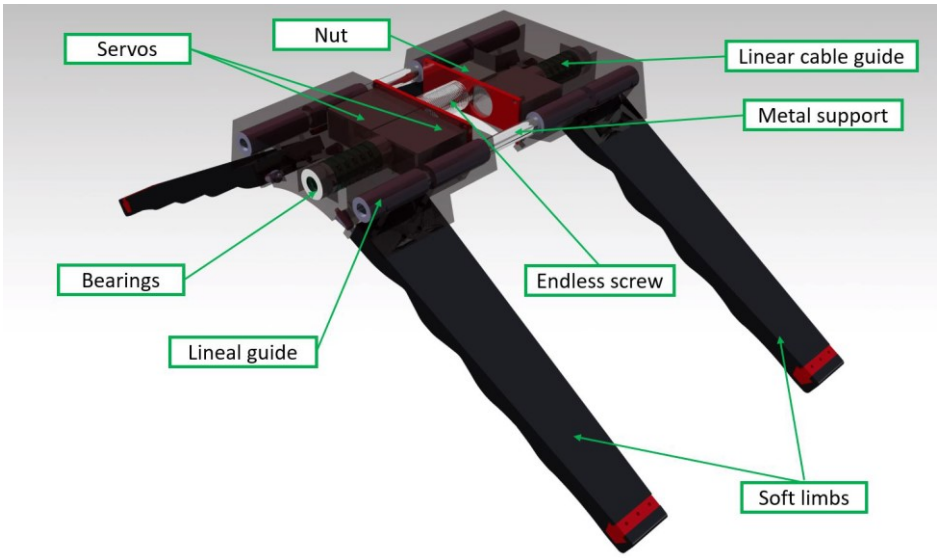

Figure 33. CAD view of the mobile soft clamp add-on.

The design of the mobile soft clamp is shown in Figure 33. The mechanism is composed of two pieces: a fixed part that is attached to the aerial platform and a mobile part that generates the forward movement. Three servomotors are responsible for all of the movements. Two of the servos are used to fold the soft limbs. The other servo actuates as an endless screw that produces the forward movement. To restrict the torsion of the endless screw, two linear guides are located at the extremes of the rigid parts, which are attached with two 8 mm bars.

The lower part of the landing gear is a half-cylindrical section for better adaptation to the pipes where it lands. The reference pipe size for this circular section is 160 mm, and the system can work in a diameter pipe range between 100 and 300 mm. On the sides, the system has two flaps protruding from the structure to attach the soft limbs.

Each limb of the mobile soft gripper is made out of TPU. This rubber-like material provides the gripper with enough rigidity to retain its shape and maintain the exerting forces, but also enough elasticity to bend and adapt to different pipe shapes. The limbs also mount a pair of PLA stiffeners and different nylon strands that exert the force to deform and obtain the circular shape of the pipe. Additionally, ecoflex elastomer is applied to the tips of the limbs to improve adhesion to the pipe, as can be seen in Figure 34.

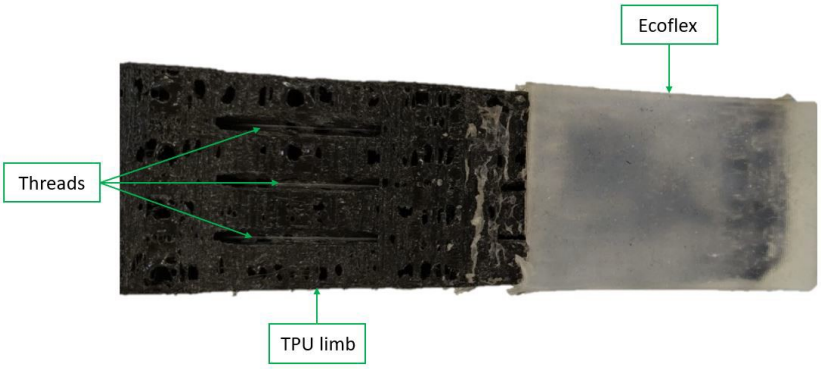

Figure 34. Fabrication of the soft limbs.

Several experiments for measuring the pressure exerted by the soft landing gear on two pipes of 140 mm and 160 mm diameter have benn done. In these experiments, force-sensing resistors (FSR sensors) have been distributed all over the soft surface (see Figure 35). These sensors have a resistance that changes when a force is applied to it. This measurement can be mapped to forces and extrapolated to pressure over the surface. Once the experiments were carried out, the data were collected and averaged to later be processed and obtain the pressure map. Figure 35 shows that more pressure is exerted in the base of the soft train and also in the tips of the limbs. The areas where less pressure is exerted are the intermediate areas due to formed folds.

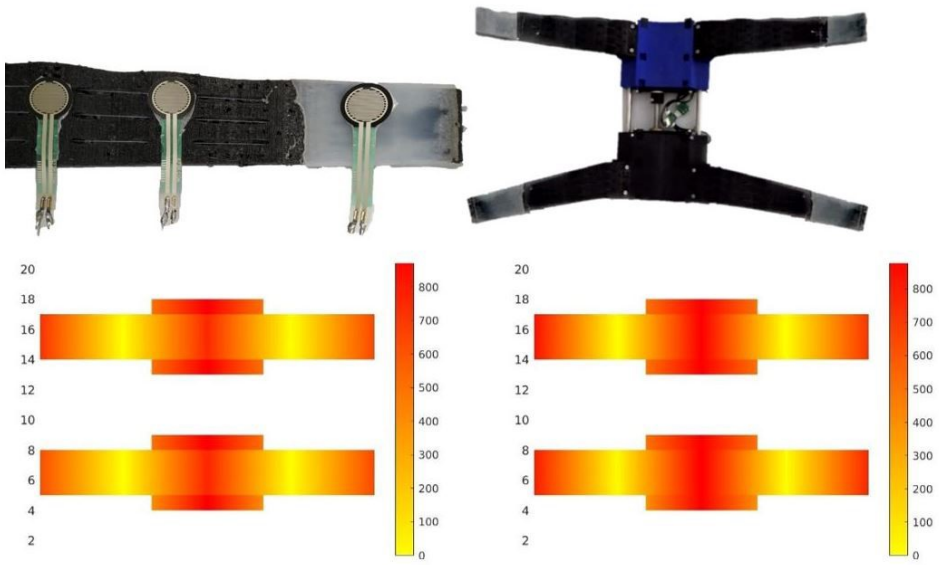

Figure 35. Pressure exerted by the mobile soft clamp on the pipe.

A study was also conducted to determine the range of the angle at which the soft train can be attached to the pipe without separating from it. For this test, a test-bench was installed in which a PVC pipe of 160 mm diameter was placed and the maximum inclination angle concerning the vertical of the pipe was checked (see Figure 36). The soft train together with the aerial platform was able to hold on to it with a maximum angle of 30º.

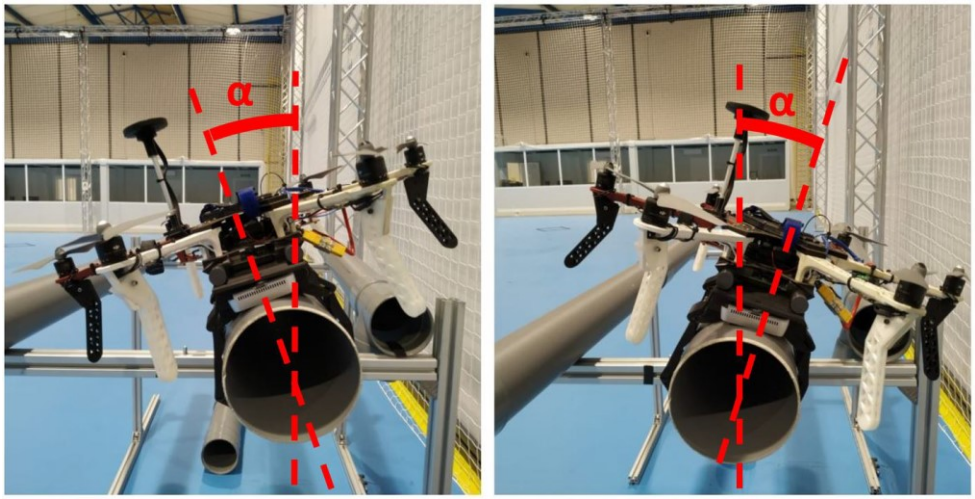

Figure 36. The maximum angle at which the landing gear can be grabbed with the drone on the pipe.

The mobile soft clamp add-on has been tested on a DJI FlameWhell 550 multirotor platform, which has a Pixhawk 2 for the control of the multirotor, an Nvidia tx2 as onboard computer, a camera connected to it to locate and position the UAV on the pipe, and a gas sensor to detect gas leaks and preventing putting the installation at risk. An AVR-based board is used to control the landing and crawling on the pipe through the controller board, which executes the program that sequentially opens and closes the soft limbs to generate the movement of the system. The AVR-based board is connected to the Nvidia tx2 onboard computer, which is in charge of sending the order received from the pilot and execute the high-level behaviour software.

Also, an ultrasonic sensor was attached to the soft landing gear to measure wall thickness of steel pipes, as it is shown in Figure 37. The ultrasonic sensor is placed at the front of the landing gear and has a motor to move the sensor up and down, to exert the right pressure so it can take the measurements.

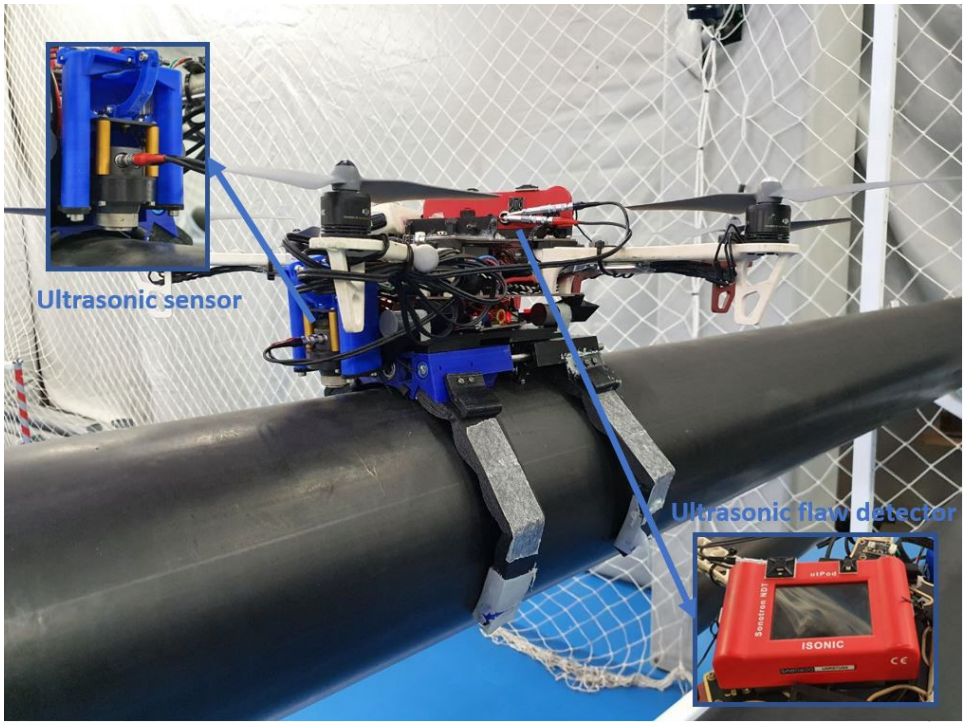

Figure 37. Aerial platform with mobile soft clamp, ultrasonic sensor and the flaw detection computer.

3.1.4. HRA final prototype

The final HRA prototype is an evolution of the aerial robot with the crawler clamp landing gear which mounts the C-Tool as manipulator for taking wall thickness measurements with the ultrasonic sensor. The final HRA prototype can be seen in Figure 38, and it is described in detail in D5.1. The final design of the landing gear which has evolved from the prototypes presented in previous sections can be seen in Figure 39.

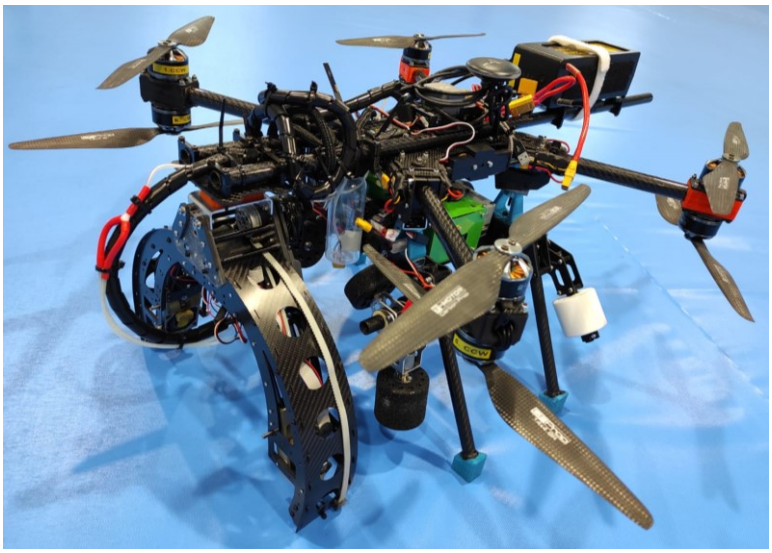

Figure 38. Complete integration of the HRA final prototype with the C-Tool.

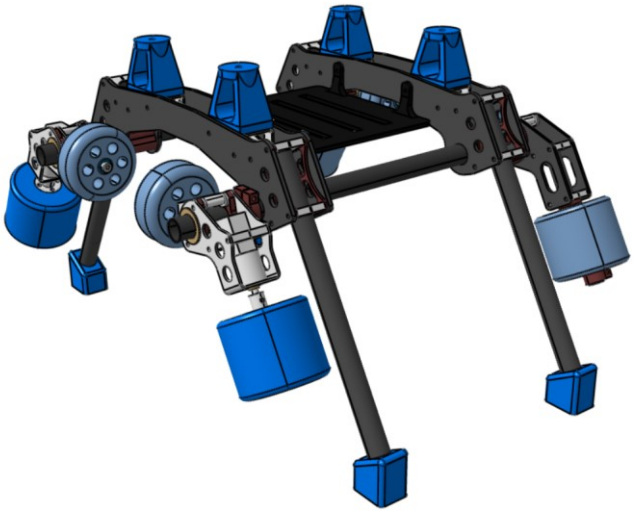

Figure 39. Final Landing Gear for Single Pipes.

3.2. HRA research exploratory concepts

This section presents three exploratory concepts that have been explored in the HYFLIERS project to develop pipe inspection technologies related to the objectives of HYFLIERS.

3.2.1. Variable pitch aerial robots

This concept is an alternative to the main HYFLIERS design line, in which once the aerial robot has landed on the pipe whole robot moves around the pipe, covering a full rotation to measure the wall thickness, avoiding the additional weight of the arm.

Stabilisation and moving around pipes and using propellers with variable pitch

The conventional multirotor design uses fixed-pitch propellers mainly due to their simpler mechanisms and easier control when compared with variable-pitch (VP) propellers. When the aerial vehicle needs to adhere to the surface of the pipe at different angles the variable-pitch solution becomes more advantageous because its ability to generate negative thrust (unlike the fixed-pitch one) becomes necessary to keep the multirotor position under circumstances such as inaccurate landing position due to wind disturbances or clearance for the gripper. Some results on the use of variable pitch rotors were presented in D2.1.

The rotation around a pipe could be modeled in two modes: one degree-of-freedom and two-DoF. In the first case, the only engaged variable is θ(rad), representative of rotation around the center of the pipe, see Fig. 1. The second case is more challenging and represents a new structure by a variable-pitch quadrotor for modeling of a rotation around the pipe with additional motion in a radial direction, r (m). Both modeling methods are logical and operational, one-DoF with a rolling clamp and the second one with additional clearance in the radial direction. The ability to provide negative thrust by VP rotors is the key to both designs.

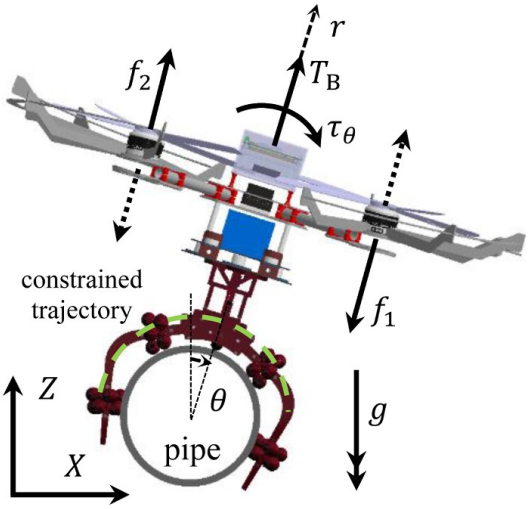

Figure 40. Schematic presentation of a quadrotor, clamping around a pipe for rotation and inspection.

A special experimental platform has been built in HYFLIERS to validate the dynamic models and control approaches [9]. The primary step is made to check the performance of the VP rotors in a controlled environment in a similar situation that resembles the pipe inspection, as presented in the schematic in Figure 40. The primary setup is presented in Figure 41. It has the option of working in two modes: one- and two-degree-of-freedom. There is a pin at the center of the setup for holding the system in one-DoF mode. If one removes the pin, the system moves in a radial r direction as well.

The setup consists of EVP-22 brushless DC (BLDC) motors with metallic variable-pitch mechanism (Figure 41-a), DJI E305 420 LITE drivers with 20A allowable current, and 17.4V allowable voltage, ES08MDII micro digital servos with 2kg.cm torque at 4.8V operating voltage. The measurement system employs optical rotary encoders LPD3806, 600 pulses per revolution with mechanical attachment to the system. The rotary motion, θ(*t*), measurement is directly made; however, the linear motion r(t) needs a customized rack and pinion design for the transformation of the linear movement to the rotation, the blue 3D printed parts in the center of the image in Figure 41-b. The digital board, responsible for communication with the computer, is an Arduino Mega 2560.

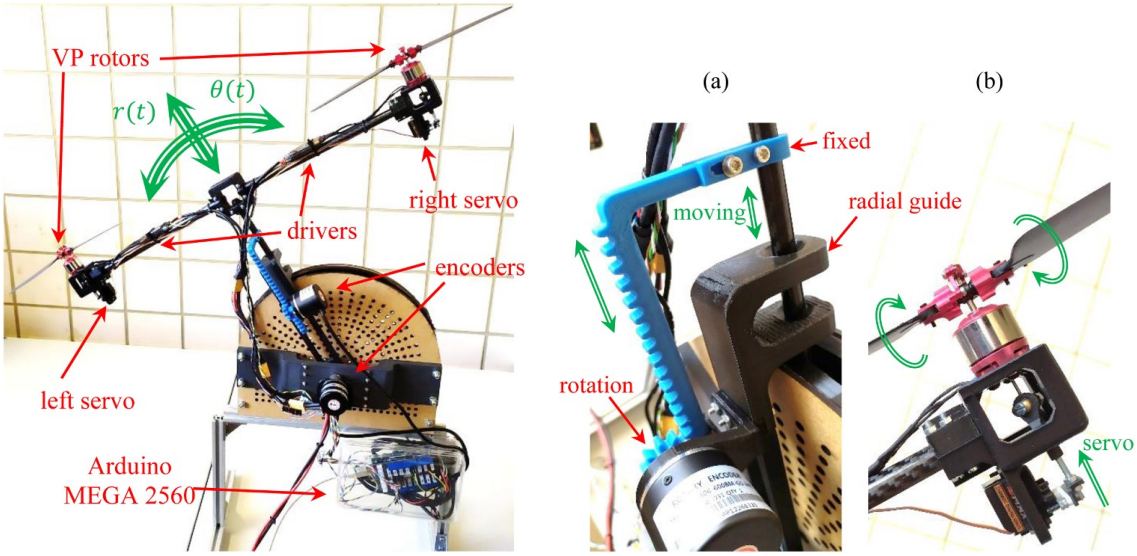

Figure 41. Experimental platform of the partial rotation around a pipe.

Next figures show the results of an experiment defined to show the capability of the system to regulate different positions in the workspace. First, the system should regulate to zero, equilibrium point, and stays there for 12s. Then regulation to +30º and -20º is required, staying around 6s at each point (see Figure 42). The variation of θ is presented also in Figure 42-a. The mapping of the input torque resulted in servo commands in Figure 42-b. A sequence of images representing the experiment is shown in Fig. 15 to illustrate different regulation points in the control task.

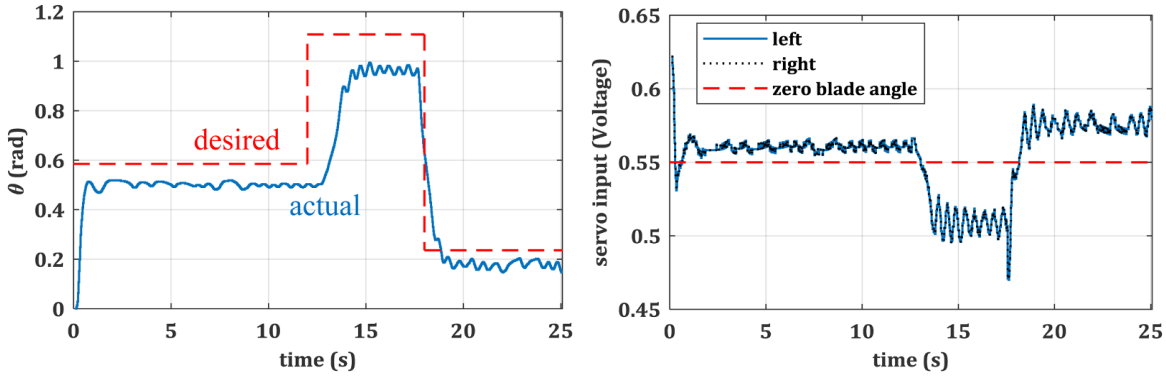

Figure 42. Reference and actual angle, and blade angles in the one-DoF experiment.

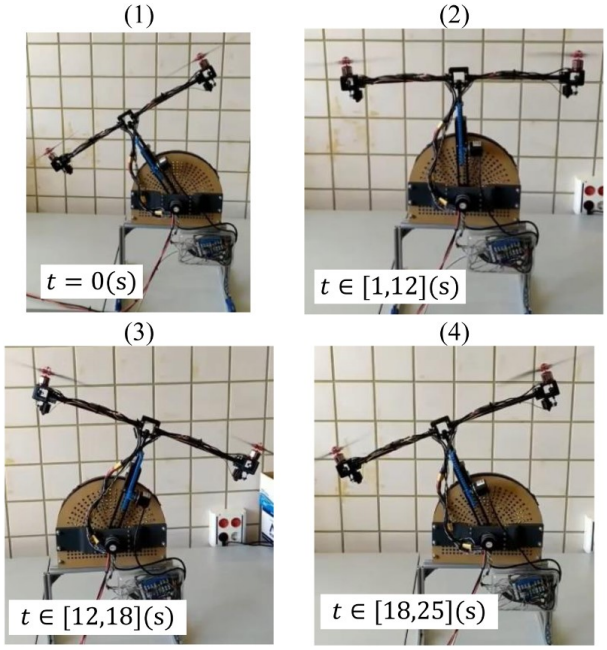

Figure 43. A sequence of images, representing the different phases of experiments; (1) system at rest, (2) regulation to equilibrium point, (3) regulation to the first point, (4) regulation to the second point.

This experimental platform has been used to test several control approaches, as the state-dependent Riccati equation closed-loop nonlinear optimal method in [9] and the (PD)-type state-dependent Riccati equation approach with iterative learning control (ILC) augmentation in [10].

Furthermore, several studies have developed in HYFLIERS for the control and stabilization of multirotors with variable pitch rotors. The papers in [11] and [12] analyse the thrust allocation of variable-pitch rotors, implementing a state-dependent Riccati equation SDRE controller for 6 DoF control of variable-pitch quadrotors.

In HYFLIERS also control strategies for manoeuvring variable-pitch rotor multirotors, which have been published in [13]. Two solutions are have been developed: the first solution uses a geometric control approach that is immune to singular points since the rotation matrix is integrated on the manifold on $SO(3)$. The second solution proposes an optimal trajectory generation for flip maneuver using open-loop optimal control, two-point boundary value problem (TPBVP) approach. Since generated open-loop state information is not applicable without a controller, the state-dependent differential Riccati equation (SDDRE) is chosen for trajectory tracking. Figure 44 shows simulations comparing the geometric controller with the SDRE controller developed in [11].

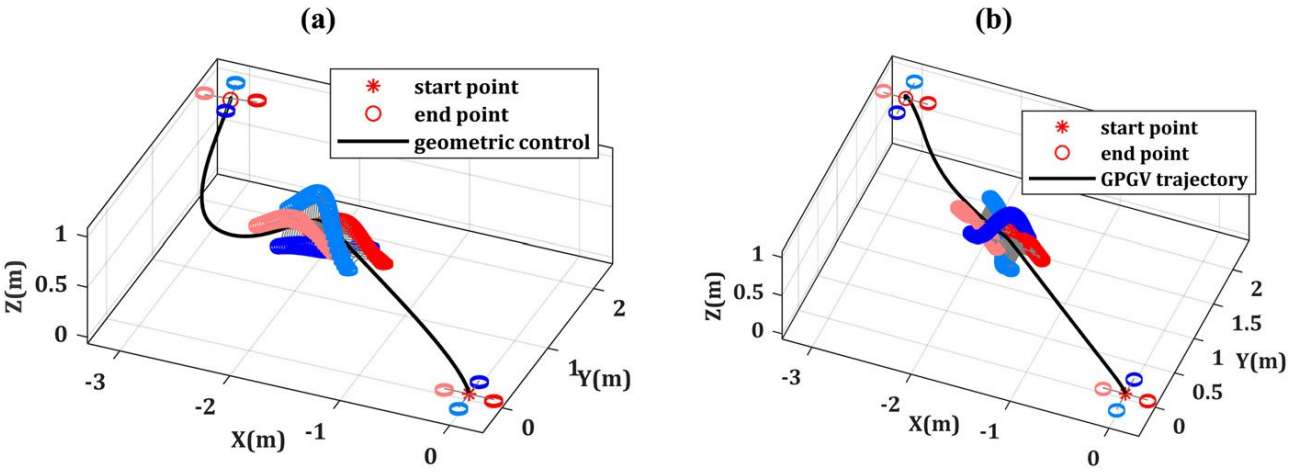

Figure 44. Flip manoeuvre of the aerial robot by (a) geometric control, and (b) SDRE controller in [11].

Furthermore, the state-dependent differential Riccati equation (SDDRE) controller has been implemented on the quaternion-based model of a multirotor allowing for singularity-free attitude representation. This work has been published in [14]. Figure 45 shows the comparison of the trajectory of the quadrotor with the proposed controller and when controlled with conventional dynamics based on Euler angles and when controlled using a proportional-derivative (PD) controller on a normal regulation flight.

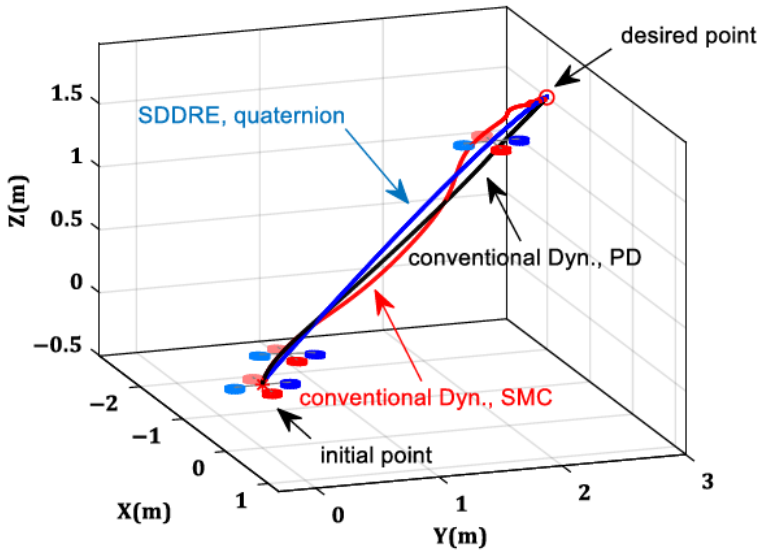

Figure 45. Quadrotor trajectories with PD, SMC, and SDDRE controllers.

Finally, the SDDRE control approach has also been applied for gravity compensation in a hexarotor with tilted rotors and published in [15]. Figure 46 shows the configuration of the tilted-rotor hexarotor and a trajectory of the hexarotor with SDDRE discrete controller.

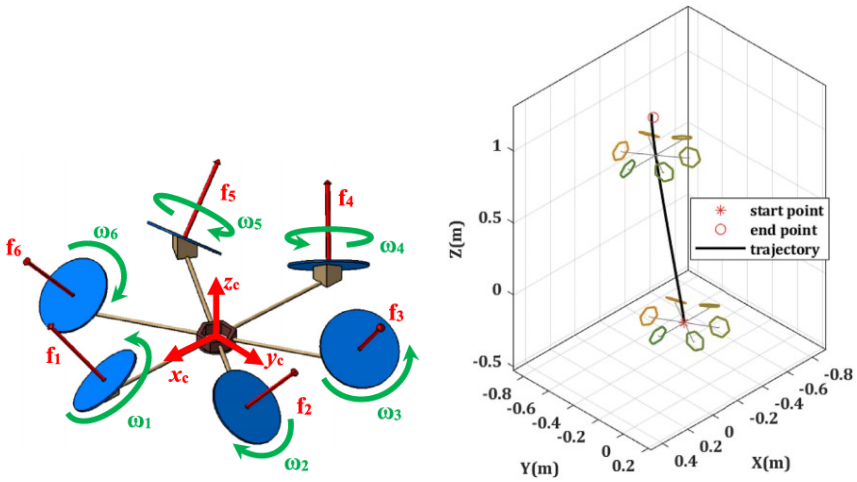

Figure 46. Configuration of the tilted-rotor hexarotor and trajectory with SDDRE discrete controller [15].

3.2.2. Soft and flexible aerial robot for pipe inspection

In HYFLIERS also has been developed the first design of a soft, 3D-printed in flexible filament, lightweight UAV, capable of performing full-body perching using soft tendons, specifically landing and stabilizing on pipes and irregular surfaces without the need for an auxiliary system. The design of the soft aerial robot can be found in [16] and [17].

The aerial robot is a modular and flexible vehicle whose entire structure is 3D-printed in flexible filament (TPU 70A) which is defined as soft by the ASTM D2240-00 standard [17]. Despite being flexible, the UAV must be able to be stable enough to carry out inspection tasks from the air, without vibrations that compromise the results. The UAV has been designed also to accomplish a safe landing on a pipe and stabilise over it without the need for any auxiliary clamping systems, only using his own deformable arms. Figure 47 shows the concept of operation of the soft aerial robot inspecting a pipe: approximation flight, landing on the pipe flexing its arms to attach to the pipe, inspection and take off.

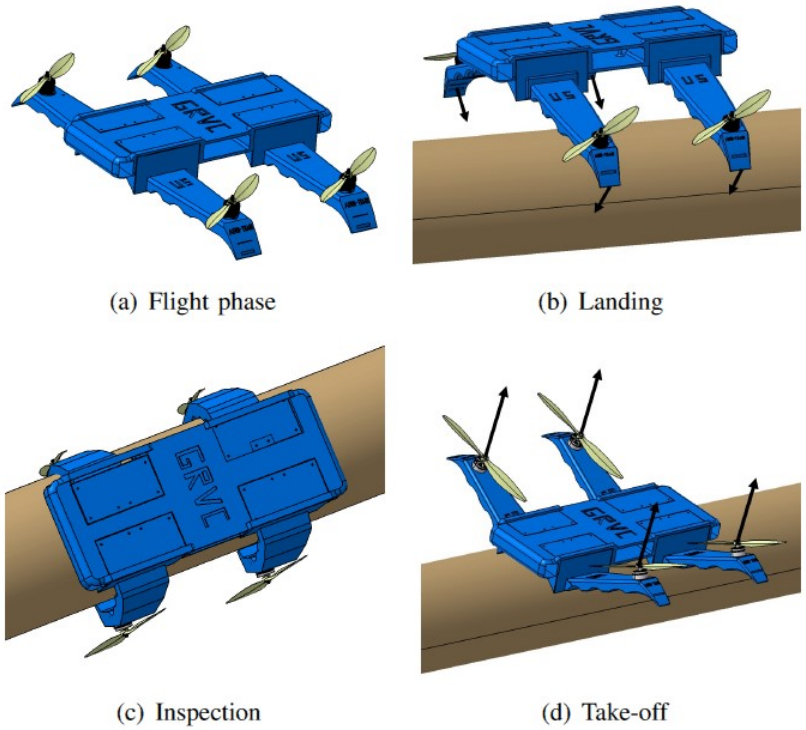

Figure 47. Concept of operation of the soft aerial robot: approximation and landing on the pipe, inspection tasks and take-off.

The prototype of the soft aerial robot that has been developed can be seen in Figure 48 in different configurations. The design of each of the four arms is presented in [16]. The propulsive equipment is composed of an electric motor (DJI 2312E), providing 450g of nominal thrust using a 4S (14.8V) battery, an electronic speed controller (DJI 430 Lite ESC) and a 10-inch DJI plastic propeller to make it safer than carbon fiber. The arm is also equipped with soft tendons on its underside, responsible for generating compression forces that cause the arm to bend downwards. These tendons are composed of nylon threads that are wound on a 3D-printed reel actuated by a HITEC MG996R servomotor which provides a maximum torque of 35 kgcm. Finally, the arm is equipped with an FSR contact force sensor from the manufacturer Interlink Electronics, which allows analyzing the level of attachment to the pipe. On the other hand, an inertial measurement unit (IMU BNo055) has been used to determine the deflection angle of the arm.

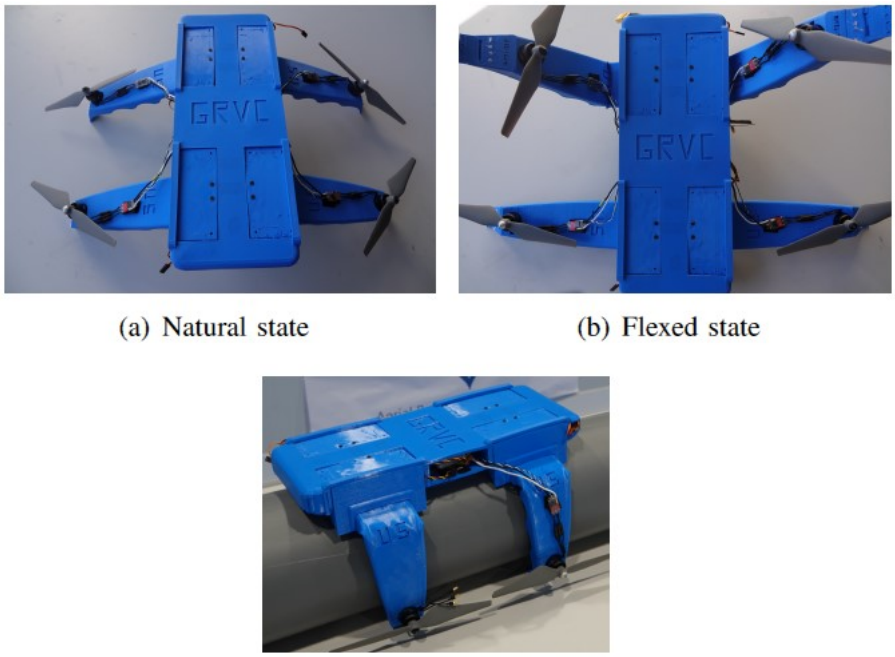

(a) Natural state (b) Flexed state

(c) Adapted to the industrial environment

Figure 48. Soft aerial robot prototype.

The design of each arm is presented in [16]. The propulsive equipment is composed of an electric motor (DJI 2312E), providing 450g of nominal thrust using a 4S (14.8V) battery, an electronic speed controller (DJI 430 Lite ESC) and a 10-inch DJI plastic propeller to make it safer than carbon fiber. The arm is also equipped with soft tendons on its underside, responsible for generating compression forces that cause the arm to bend downwards. These tendons are composed of nylon threads that are wound on a 3D-printed reel actuated by a HITEC MG996R servomotor which provides a maximum torque of 35 kgcm. Finally, the arm is equipped with an FSR contact force sensor from the manufacturer Interlink Electronics, which allows analyzing the level of attachment to the pipe. On the other hand, an inertial measurement unit (IMU BNo055) has been used to determine the deflection angle of the arm.

3.2.3. Aerial robot with docking tool for pipe inspection

Another concept that we have explored in HYFLIERS is the inspection of the pipes while flying, with an arm that touches the pipe and maintains the relative position of the aerial robot with the pipe, while taking measurements with the sensors in contact with the pipe. Figure 49 shows two aerial robots touching the pipes with the docking tool while flying close to them. This work has been published in the Robotics & Automation Magazine [18].

Figure 49. Aerial robots with docking tool attached to pipes.

3.3. HRA autonomous functionalities

3.3.1. Pipe detection from the aerial robot

In the project it has been developed a pipe detection framework using a visual algorithm based on a semantic convolutional neuronal network, which can be found in [7]. The information from a color camera is used to segment the image. Then, the segmentation information is fused with a depth image to estimate the pipe's pose, so that the pose of the robot can be controlled relative to it.

The main visual sensor of the system is an Intel RealSense D435. This camera has excellent performance in outdoor environments with great resolution, making it adequate for the project. The camera is positioned under the UAV, in an overhead position so that the vision of the pipe is clear.

The detection algorithm uses the color and depth images obtained from the Intel RealSense D435 device. The detection occurs in two stages. At first instance, a convolutional neural network uses the color image to perform the segmentation. Then, the segmentation is used with the depth image to estimate the pose of the target pipe accurately. As aforementioned, a convolutional neural network is used. The idea behind it is the fact that grouped convolutions and shuffled channels reduce computational cost while maintaining good accuracy.

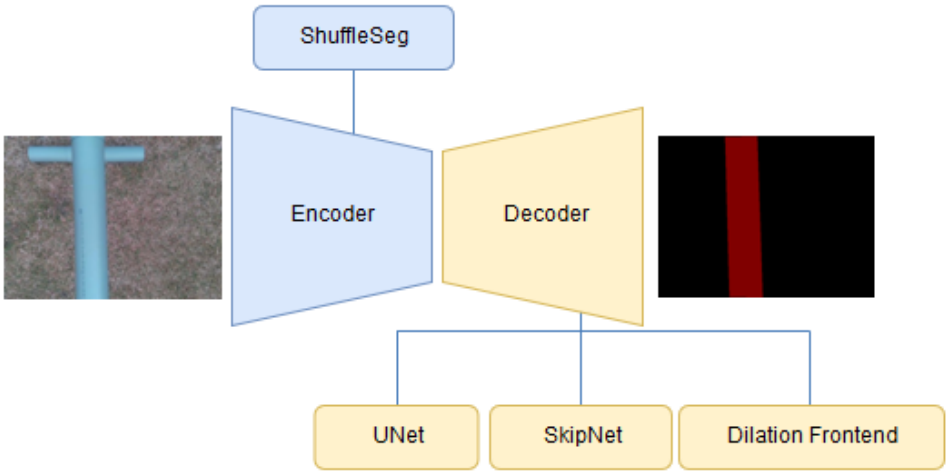

Figure 50. Graph showing the Encoder/Decoder structure of the neural network.

As seen in Figure 50, the network has an Encoder-Decoder structure that is fed with the color images and outputs a segmented image with the same size. The Shuffleseg encoder structure has been chosen because of its speed. For the decoder structure, three options have been implemented: UNet, SkipNet and Dilation Frontend. The selection of this network fragment compromises the trade-off between the accuracy and the speed of the system.

The result of the network is a mask image, of the same size of the input image, with the segmentation of the different classes. This mask corresponds to the argmax function of the probability of the classes. In this case, only two classes are searched. The pipe and the background, which will be all the other parts of the image and will be shown as black at the output image.

Figure 51 shows example results of the pipe detection system, with the detected pipe marked in red in the las image.

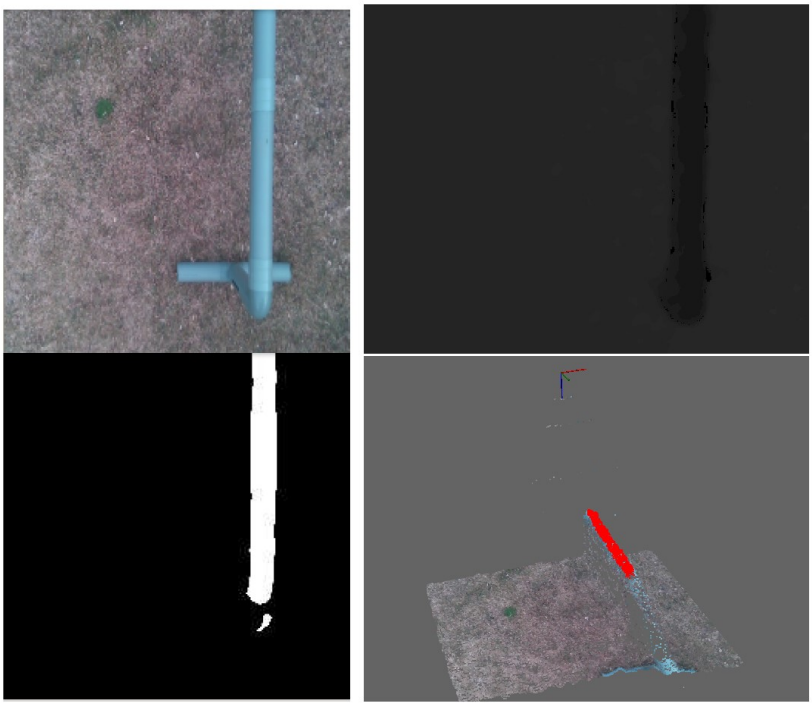

Figure 51. Top images show the input frames from the Intel RealSense device. Bottom figures show respectively the argmax result from the CNN and the detection from the RANSAC algorithm, which highlights the result in red.

Furthermore, a solution for short-range pipe detection based on low-cost sensors has also been explored, and presented in [19]. The system is based on Time of Flight (ToF) sensors that measure the relative distance to the pipe at different points. The system consists of two linear arrays of distance sensors whose orientation angle is controlled to track the contour of the pipe, providing an estimation of the relative position and orientation. Figure 52 shows the principle of operation and the prototype that has been built. Experimental results can be found in [19].

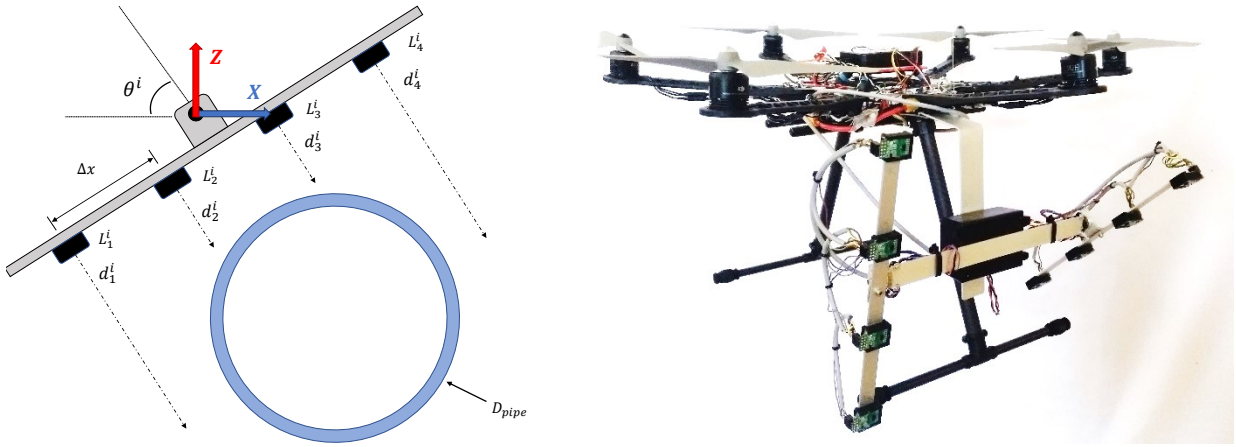

Figure 52. Short-range pipe positioning system: a) principle of operation, b) prototype mounted on a multirotor.

3.3.2. Aerodynamic interaction with pipes

The use of aerial robotic systems for manipulation tasks usually requires that rotors operate in the proximity of surfaces that can affect their airflow. This is the case of the aerial robots in HYFLIERS, which have to fly close and land on pipes or racks of pipes. Working under such conditions leads to aerodynamic phenomena that can provoke destabilisations or even crashes. In order to avoid these dangerous flight conditions, the compensation of aerodynamic effects should be considered in the design of the controller or taken into account in the trajectory generation process of the motion planner.

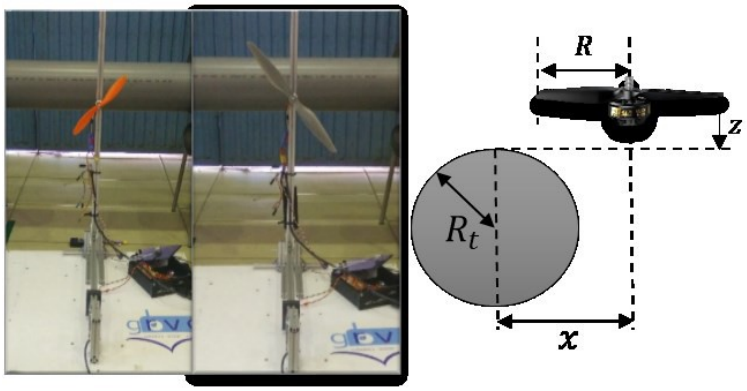

Figure 53. Experimental testbed for estimation of aerodynamic interference.

In HYFLIERS we have done experiments to model the different aerodynamic interactions that occur when flying in refineries. This work has been published in [20] and [21]. Figure 56 shows the experimental testbed used for characterization of the interaction. Figure 54 presents the results of the experiments for different relative positions of the rotors and pipes, when flying above or below the pipe, and Figure 55 shows an example aerodynamic map of an environment with three pipes.

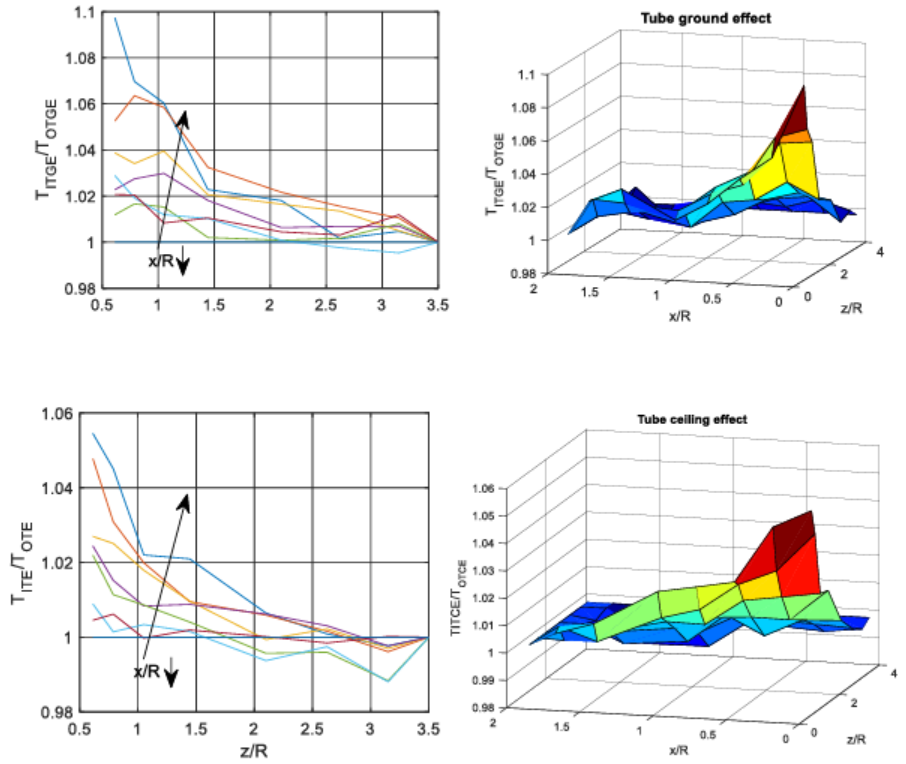

Figure 54. Results of the aerodynamic interference experiments.

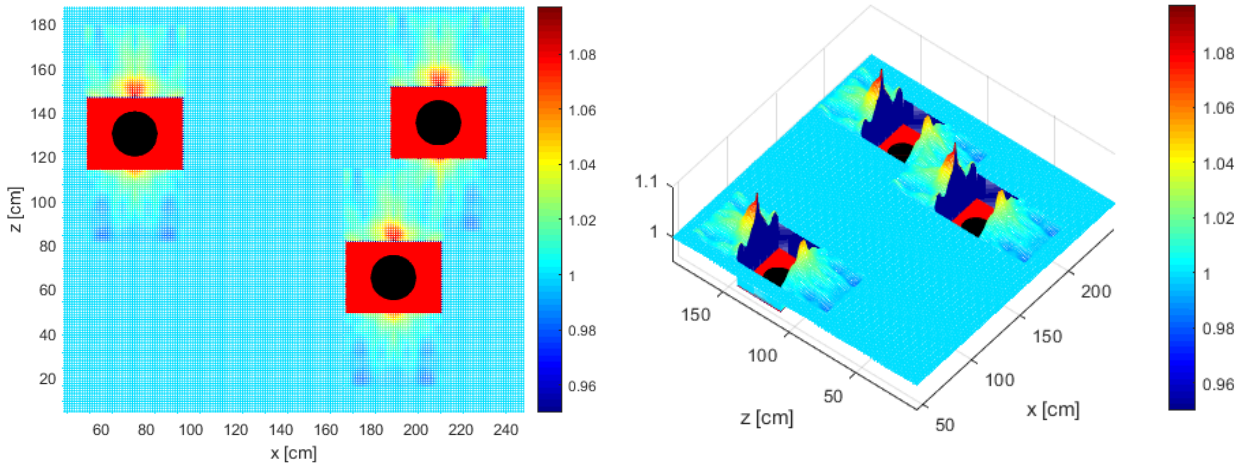

Figure 55. Aerodynamic interference map of a scenario with three pipes.

3.3.3. HRA autonomous landing on pipe racks

One of the tasks in HYFLIERS is landing on a rack of pipes for inspection, mainly measurement of the pipe thickness and corrosion. The rack of pipes generates an unknown disturbance caused by the induced airflow by the propellers during the landing phase. The ground effect modeling for flat surfaces is straight forward; however, the rack of pipes imposes more uncertainty on the system modeling. The source of aerodynamics disturbance also could be either external wind or the one caused by the UAV's propellers near the pipes or ground. This section presents a solution for the one-

shot landing of the HRA on a rack of pipes considering the ground effect. The work presented here has been published in [22] and [23].

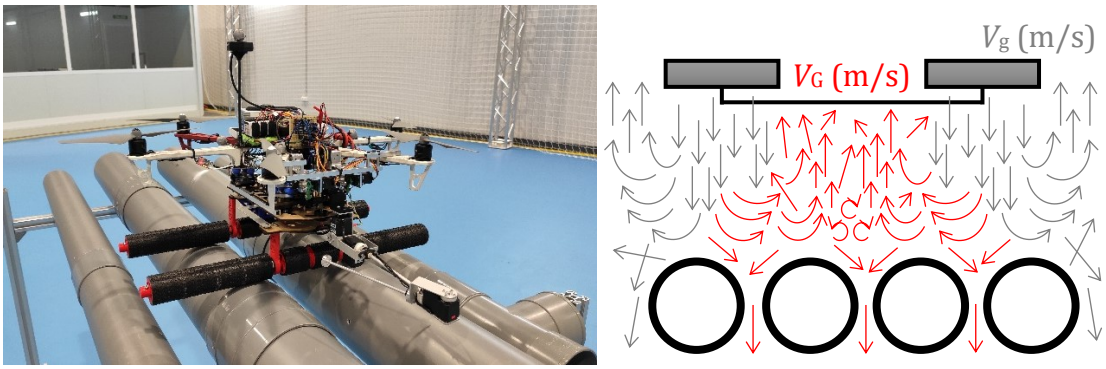

Figure 56. a) HRA with rollers landing gear on pipe rack; b) airflow modelling.

The controller presented in this section is based on the modelling the airflow around the multirotor and the pipes, as represented in Figure 56. There are three airflow velocities: V_o the airflow speed far from the ground, V_g the airflow speed near the ground, and the reflection of airflow by the ground

The system is free in normal flying far from the ground. In case that the quadrotor approaches the ground two airflows will be built, one flow toward the outside of the system and one airflow toward the inside. Computation of the inward airflow speed, so-called V_G is the objective of this section. The ground effect for propeller systems was proposed to define a relation for calculating the thrust near the ground based on the image method. The relation for a single rotor is:

$$\frac{T_g}{T_B} = \frac{1}{1 - \left(\frac{R}{4z_c}\right)^2}$$

where T_B (N) is the thrust of the propeller in free flight, T_g (N) is the thrust under the ground effect, R (m) is the radius of the propeller and z_c (m) is the distance of the rotor from the ground. Increasing the number of rotors to four, reforms the equation to:

$$\frac{T_g}{T_B} = \frac{1}{1 - \left(\frac{R}{4z_c}\right)^2 - \frac{R^2 z_c}{\sqrt{(d + 4z_c^2)^3}} - \frac{R^2 z_c}{2\sqrt{(2d + 4z_c^2)^3}}}.$$

From that we could represent the ground reflection of wind with direction towards the ground, $-Z$, which causes the negative sign for V_g:

$$V_g = -V_o \frac{1}{\sqrt{1 - \left(\frac{R}{4z_c}\right)^2 - \frac{R^2 z_c}{\sqrt{(d + 4z_c^2)^3}} - \frac{R^2 z_c}{2\sqrt{(2d + 4z_c^2)^3}}}}$$

The *effective* distance between the quadcopter and the ground for studying the ground effect was reported dist. $= 5R$. So, if the system is higher than $5R$, the effect of the ground is zero and the UAV flies normally. It can be defined that $V_G(5R) = 0$ and $V_G(0) = V_g$, though the behavior of airflow

between the two boundary values is not defined. Assuming a linear relation between two boundary values and present $V_{\mathrm{G}} = -\frac{V_{\mathrm{g}}}{5R} z_{\mathrm{c}} + V_{\mathrm{g}}$ in domain of $z_{\mathrm{c}} \in [0, 5R]$. Based on the direction of the ground reaction, the ultimate airflow speed by the ground is

$$\begin{cases} V_{\mathrm{G}} = \dfrac{V_{\mathrm{g}}}{5R} z_{\mathrm{c}} - V_{\mathrm{g}}, & z_{\mathrm{c}} \in [0, 5R], \\ 0 & z_{\mathrm{c}} > 5R. \end{cases}$$

This equation implies that the high-speed reaction by the ground is generated near the ground and increases the thrust of the UAV. Landing in this condition faces a couple of bumps before turning off the rotors and removing the thrust. To present a smooth soft landing, without any special landing gear, or better to say one-shot landing, the produced wind reflection by the ground must be considered in the control design and modeling of the system.

A sliding mode controller has been designed and tested in simulation, the complete derivation can be found in [22].

Also, a practical implementation has been done in HYFLIERS with a multirotor with a modified autopilot implementing a state-dependent scalar gain $K_{p_z}(x)$ for thrust reduction near the ground based on the wind modeling approach. We define a feedforward reduction term

$$\mathbf{S}(\mathbf{x}) = -\hat{\mathbf{v}}_2(\mathbf{v}_1 + \mathbf{W}_{\mathrm{c}}) - \dot{\mathbf{W}}_{\mathrm{c}},$$

from translational dynamics, which reduces the thrust near the landing. If we substitute the third component of $S(x)$ into the proportional gain with scaling factor α, we will find a new proportional gain as:

$$K_{\mathrm{P},z}(\mathbf{x}) = K_{\mathrm{P},z} + \alpha S_z(\mathbf{x}),$$

where α scales the $S_z(x)$ in the overall gain. So, it can be realized that the gain is constant in all workspace, and $S_z(x)$ will be activated in $z_c \in [0, 5R]$ reducing the $K_{p_z}(x)$ with the tuning parameter α.

These developments have been published in [23], and Figure 57 shows the results of several experimental tests with different values of α ranging from 0 to 1000. The best performance was gained by $\alpha = 750$.

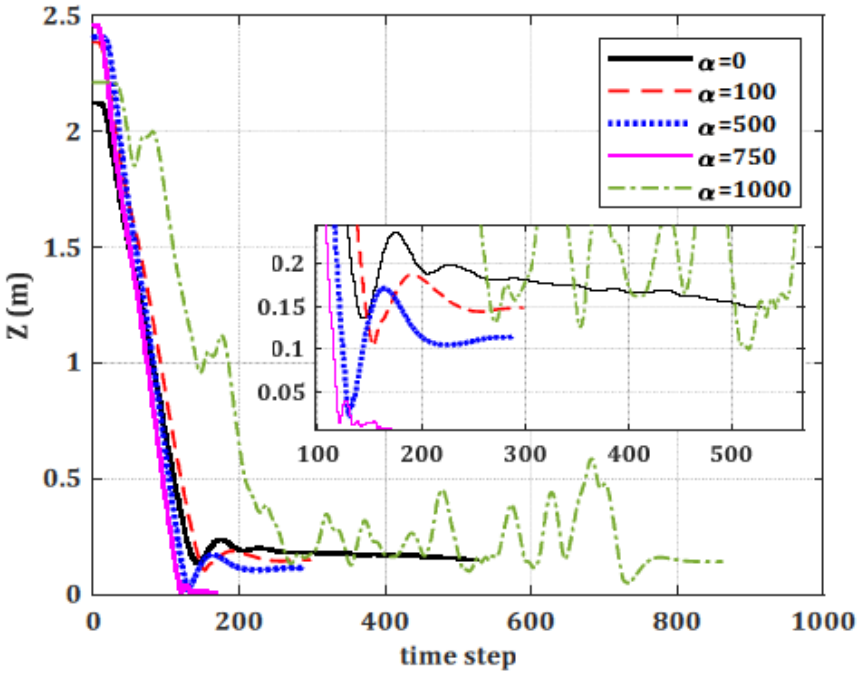

Figure 57. Results of soft landing with different values of α.

4. Conclusions

This document has presented the design of the HYFLIERS hybrid robot prototypes, the HMR and the HRA. The deliverable has presented the evolution of the design of both robots, from the first prototypes to the modifications and improvements developed with the experience gained along the project. Several research concepts that have been explored in the framework of HYFLIERS are also included in the document.

With this deliverable concludes the exploratory research developed in HYFLIERS. The final integrated versions of the HMR and HRA robots and their components will be presented in D5.1 and D5.2.

References

HYFLIERS publications

[1] M. A. Montes-Grova, F. J. Perez-Grau and A. Viguria. “Multi-Sensor System for Pipe Inspection using an Autonomous Hybrid Aerial Robot”. *International Conference on Unmanned Aircraft Systems*, June 2022, Dubrovnik, Croatia.

[2] M. Salvago, F. J. Perez-Gran, J. Parra, M. A. Trujillo, and A. Viguria. “Robust and efficient pose estimation of pipes for contact inspection using aerial robots”, 2021 Aerial Robotic Systems Physically Interacting with the Environment (AIRPHARO), pp. 1–6, 2021.

[3] A. Lopez-Lora, P. J. Sanchez-Cuevas, A. Suarez, A. Garofano-Soldado, A. Ollero and G. Heredia, "MHYRO: Modular HYbrid RObot for contact inspection and maintenance in oil & gas plants," 2020 IEEE/RSJ International Conference on Intelligent Robots and Systems (IROS), 2020, pp. 1268-1275, https://doi.org/10.1109/IROS45743.2020.9341639. *IROS 2020 Best Application Paper Award*.

[4] F. J. Garcia-Rubiales, P. Ramon-Soria, B. C. Arrue and A. Ollero, "Magnetic detaching system for Modular UAVs with perching capabilities in industrial environments," 2019 Workshop on Research, Education and Development of Unmanned Aerial Systems (RED UAS), 2019, pp. 172-176, https://doi.org/10.1109/REDUAS47371.2019.8999704.

[5] A. Suarez, M. Perez, G. Heredia and A. Ollero, “Cartesian Aerial Manipulator with Compliant Arm”. Appl. Sci. 2021, 11, 1001. https://doi.org/10.3390/app11031001.

[6] A. Suarez, A. Caballero, A. Garofano, P. J. Sanchez-Cuevas, G. Heredia and A. Ollero, "Aerial Manipulator With Rolling Base for Inspection of Pipe Arrays," IEEE Access, vol. 8, pp. 162516-162532, 2020, https://doi.org/10.1109/ACCESS.2020.3021126.

[7] P. Ramon-Soria, A. E. Gomez-Tamm, F. J. Garcia-Rubiales, B. C. Arrue and A. Ollero, "Autonomous landing on pipes using soft gripper for inspection and maintenance in outdoor environments," 2019 IEEE/RSJ International Conference on Intelligent Robots and Systems (IROS), 2019, pp. 5832-5839, https://doi.org/10.1109/IROS40897.2019.8967850.

[8] F.J. Garcia-Rubiales, P. Ramon-Soria, B.C. Arrue and A. Ollero, “Soft-Tentacle Gripper for Pipe Crawling to Inspect Industrial Facilities Using UAVs”, Sensors 2021, 21, 4142. https://doi.org/10.3390/s21124142.

[9] S. R. Nekoo, J. Á. Acosta, G. Heredia and A. Ollero, “A benchmark mechatronics platform to assess the inspection around pipes with variable pitch quadrotor for industrial sites”, Mechatronics, Vol. 79, 2021, Art 102641, https://doi.org/10.1016/j.mechatronics.2021.102641.

[10] S. R. Nekoo, J. Á. Acosta, G. Heredia and A. Ollero, "A PD-Type State-Dependent Riccati Equation with Iterative Learning Augmentation for Mechanical Systems," in IEEE/CAA Journal of Automatica Sinica, vol. 9, no. 8, pp. 1499-1511, August 2022, doi: https://doi.org/10.1109/JAS.2022.105533.

[11] S. R. Nekoo, J. Á. Acosta, A. E. Gomez-Tamm and A. Ollero, "Optimized Thrust Allocation of Variable-pitch Propellers Quadrotor Control: A Comparative Study on Flip Maneuver," 2019 Workshop on Research, Education and Development of Unmanned Aerial Systems (RED UAS), 2019, pp. 86-95, https://doi.org/10.1109/REDUAS47371.2019.8999681.

[12] S. R. Nekoo, J. Á. Acosta and A. Ollero, "Fully Coupled Six-DoF Nonlinear Suboptimal Control of a Quadrotor: Application to Variable-Pitch Rotor Design”. In: Silva, M., Luís Lima, J., Reis, L., Sanfeliu, A., Tardioli, D. (eds) Robot 2019: Fourth Iberian Robotics

Conference. ROBOT 2019. Advances in Intelligent Systems and Computing, vol 1093. Springer, Cham, 2020. https://doi.org/10.1007/978-3-030-36150-1_7.

[13]S. R. Nekoo, J. Á. Acosta and A. Ollero, "Geometric control using the state-dependent Riccati equation: application to aerial-acrobatic maneuvers", International Journal of Control, 95:7, 1875-1887, 2022, https://doi.org/10.1080/00207179.2021.1881165.

[14]S. R. Nekoo, J. Á. Acosta and A. Ollero, "Quaternion-based state-dependent differential Riccati equation for quadrotor drones: Regulation control problem in aerobatic flight", Robotica, 40(9), 3120-3135, 2022, https://doi.org/10.1017/S0263574722000091.

[15]S. R. Nekoo, J. Á. Acosta and A. Ollero, "Gravity compensation and optimal control of actuated multibody system dynamics", IET Control Theory Appl. 16, 79– 93, 2022, https://doi.org/10.1049/cth2.12206.

[16]F. Ruiz, B. Arrue and A. Ollero, "A flexible propelled arm: Mechanical considerations for the use in UAVs," 2022 International Conference on Unmanned Aircraft Systems (ICUAS), 2022, pp. 1047-1055, https://doi.org/10.1109/ICUAS54217.2022.9836149.

[17]F. Ruiz, B. C. Arrue and A. Ollero, "SOPHIE: Soft and Flexible Aerial Vehicle for Physical Interaction with the Environment," IEEE Robotics and Automation Letters, vol. 7, no. 4, pp. 11086-11093, Oct. 2022, https://doi.org/10.1109/LRA.2022.3196768.

[18]P. Ramon-Soria, B. C. Arrue and A. Ollero, "A 3D-Printable Docking System for Aerial Robots: Controlling Aerial Robotic Manipulators in Outdoor Industrial Applications," in *IEEE Robotics & Automation Magazine*, vol. 26, no. 1, pp. 44-53, March 2019, https://doi.org/10.1109/MRA.2018.2884744.

[19]M. Perez, A. Suarez, G. Heredia and A. Ollero, "Positioning System for Pipe Inspection with Aerial Robots Using Time of Flight Sensors". In: Silva, M., Luís Lima, J., Reis, L., Sanfeliu, A., Tardioli, D. (eds) Robot 2019: Fourth Iberian Robotics Conference. Advances in Intelligent Systems and Computing, vol 1092. Springer, Cham. https://doi.org/10.1007/978-3-030-35990-4_2.

[20]P. J. Sanchez-Cuevas, V. Martín, G. Heredia and A. Ollero, "Aerodynamic Effects in Multirotors Flying Close to Obstacles: Modelling and Mapping". In: Silva, M., Luís Lima, J., Reis, L., Sanfeliu, A., Tardioli, D. (eds) Robot 2019: Fourth Iberian Robotics Conference. Advances in Intelligent Systems and Computing, vol 1092. Springer, Cham. https://doi.org/10.1007/978-3-030-35990-4_6.

[21]A. Caballero, P. J. Sanchez-Cuevas, M. Bejar, G. Heredia, M. A. Trujillo and A. Ollero, "An Aerodynamic Extension for Motion Planning with Dynamics Awareness in Aerial Long-Reach Manipulators", International Journal of Aerospace Engineering, vol. 2020, Article ID 6348035, 17 pages, 2020. https://doi.org/10.1155/2020/6348035.

[22]S. R. Nekoo, J. Á. Acosta, G. Heredia and A. Ollero, "Soft-Landing of Multi-Rotor Drones using a Robust Nonlinear Control and Wind Modeling," 2021 International Conference on Unmanned Aircraft Systems (ICUAS), 2021, pp. 1070-1079, https://doi.org/10.1109/ICUAS51884.2021.9476763.

[23]S. R. Nekoo, P. J. Sanchez Cuevas, J. Á. Acosta, G. Heredia and A. Ollero, "Experimental Investigation of Soft-Landing of Quadrotors via Induced Wind Modeling Approach," 2021 Aerial Robotic Systems Physically Interacting with the Environment (AIRPHARO), 2021, pp. 1-6, https://doi.org/10.1109/AIRPHARO52252.2021.9571054.

[24]S. R. Nekoo, J. Á. Acosta and A. Ollero, "Collision Avoidance of SDRE Controller using Artificial Potential Field Method: Application to Aerial Robotics," 2020 International Conference on Unmanned Aircraft Systems (ICUAS), 2020, pp. 551-556, https://doi.org/10.1109/ICUAS48674.2020.9213984.

Other references

[25]Michael Grupp. evo: Python package for the evaluation of odometry and slam. https://github.com/MichaelGrupp/evo, 2017.

[26]Radu Bogdan Rusu and Steve Cousins. 3D is here: Point Cloud Library (PCL). In IEEE International Conference on Robotics and Automation (ICRA), Shanghai, China, May 9-13 201.

[27]Rohit Chandra, Leo Dagum, David Kohr, Ramesh Menon, Dror Maydan, and Jeff McDonald. Parallel programming in OpenMP. Morgan kaufmann, 2001.

[28]Martin A. Fischler and Robert C. Bolles. Random sample consensus: a paradigm for model fitting with applications to image analysis and automated cartography. Commun. ACM, 24:381–395, 1981.

[29]Lars-Alexander Albrecht. Curvature-based analysis of point clouds. Fakulta¨t Informatik, Elektrotechnik und Informationstechnik, 2014.

[30]A. Suarez, G. Heredia and A. Ollero, “Design of an anthropomorphic, compliant, and lightweight dual arm for aerial manipulation” IEEE Access, vol. 6, pp. 29173-29189, 2018.